

Chapter 5¹

Deep Space Station 14: Mars

The need for large-aperture, ground-based antennas with greater capability than the previously existing 26-m-diameter antennas was foreseen and documented in early 1960. An outgrowth of this need was the Advanced Antenna System (AAS) Project [1] to design, build, and initially operate a 64-m antenna at the Deep Space Communications Complex (DSCC) in Goldstone, California. The antenna was inaugurated with the tracking of the Mariner 4 spacecraft as it was occulted by the Sun in April 1966 and, as there was a tradition to name Deep Space Network (DSN) antennas for their first operational activity, the new antenna was designated the Mars antenna. Ultimately, two more antennas of the same design were built for Spain and Australia.

Whereas the 64-m antenna was a significant advancement mechanically over existing antennas, the radio frequency (RF) design was initially a simple scaling of the highly successful systems that had been previously utilized on the DSN 26-m antennas. For the 64-m antenna, the Cassegrain geometry was chosen to be a physical scale of the 26-m Cassegrain design, allowing interchangeability of the feed-horn structures and permitting test of the feed horns on a 26-m antenna prior to commitment for use on the 64-m antenna.

In Fig. 5-1, the 64-m antenna, which featured a fully steerable azimuth–elevation mount, is shown at the time of its initial operation; Fig. 5-2 details the major components of the antenna system.

¹Based on “Evolution of the Large Deep Space Network Antennas,” by William A. Imbriale, which appeared in *IEEE Antennas & Propagation Magazine*, vol. 33, no. 6, December 1991. (© 1991 IEEE)



Fig. 5-1. The 64-m antenna at the time of initial operation.

The tipping structure contains the significant RF components: the primary reflector surface, the secondary hyperboloidal reflector surface, a supporting quadripod structure, and a Cassegrain feed-horn support.

This chapter describes the evolution in performance, from 1966 to 2001, of the largest DSN antenna: the size increase from 64 to 70 m; enhanced efficiencies through dual-reflector shaping; operational frequency upgrade from S-band (2.110–2.120 GHz transmit and 2.290–2.300 receive) to X-band (7.145–7.190 transmit and 8.400–8.450 receive), with a plan for future Ka-band (34.200–34.700 transmit and 31.800–32.300 receive); and growth from single-frequency to multifrequency operation. Design, performance analysis, and measurement techniques are highlighted.

5.1 Antenna Structure

The primary reflector structure was a 64-m-diameter paraboloidal space frame supported by a truss-type backup structure. The space frame was a network of 48 rib trusses radiating from the center hub and interconnected by a rectangular girder, intermediate rib trusses, and ten circular hoop trusses. The backup structure was formed by two elevation-wheel trusses, supported and braced by a tie truss. Elevation-wheel trusses supported the elevation-gear seg-

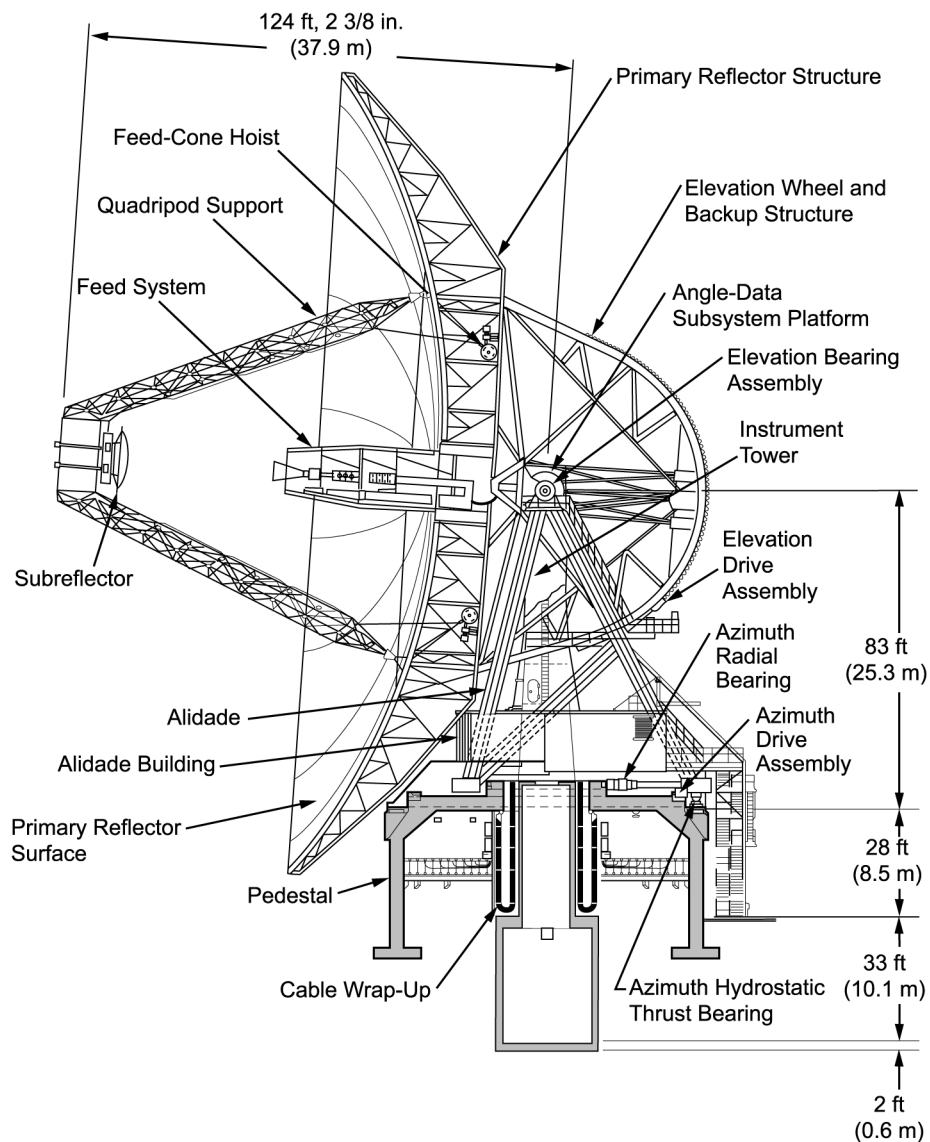


Fig. 5-2. Tipping structure of the 64-m antenna, showing major components.

ments, and counterweights were placed to statically balance the tipping assembly about the elevation axis.

The surface of the primary reflector comprised 552 individual panels contoured from aluminum sheet and riveted to a precisely formed aluminum frame. The panels were affixed to the reflector backup structure with adjusting screws that were accessible from the exposed surface of the reflector; the design is such that loads in the backup structure were not transmitted into the surface

panels. Together, the panels formed a solid reflecting surface over the inner half-radius of the reflector and a perforated surface over the outer half-radius.

The quadripod that supported the subreflector was a tubular space-frame structure of four trapezoidally shaped legs meeting in a large-apex space frame. The four legs were supported at the hard points of the rectangular girder in the primary reflector structure. The quadripod also supported pulleys and/or hoists for handling the Cassegrain feed horns, the subreflector, or other heavy equipment being brought to or from the reflector, with the elevation motion of the quadripod legs acting as a crane.

The subreflector was a precision hyperboloidal reflecting surface 20 ft (6.1 m) in diameter, with a 12-in. (305-mm) radial flange for improving the microwave feed system. A hub and backup space-frame structure were designed with linear adjustment capability provided by remotely controlled electric motors and screwjack assemblies.

The Cassegrain feed-horn support (Fig. 5-3) was a large, three-module structure used to mount the actual feed horn and to house the receiver and transmitter equipment. The lower module was an open-framed steel truss (this

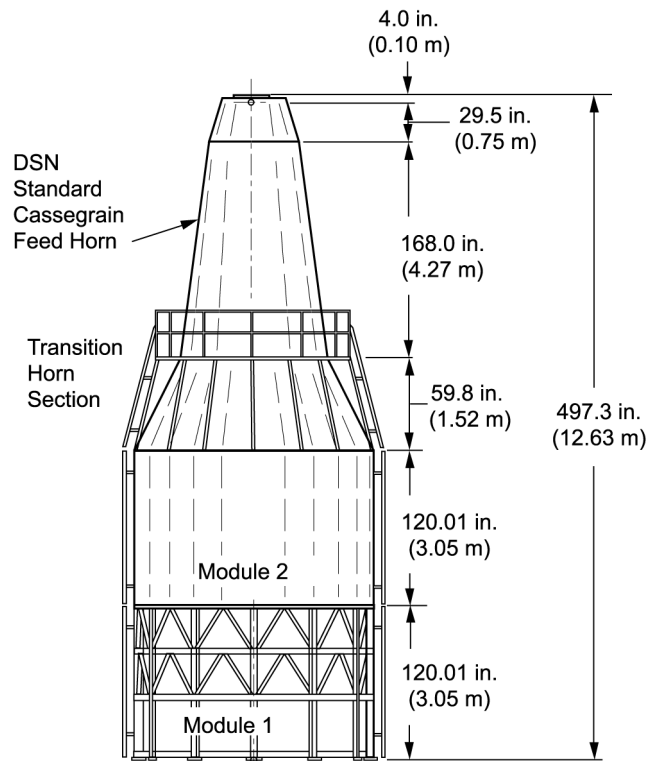


Fig. 5-3. Feed-horn configuration during initial antenna operations.

allowed optical surveys of the reflector surface), attached to the center hub of the primary reflector structure. The center module was a framed, stressed-skin cylinder that provided a controlled environment area for microwave and electronics equipment. The upper module was a framed, stressed-skin truncated cone that provided a more controlled environment for equipment. The upper module also contained the Cassegrain feed-horn adapter, designed to permit use of any standard DSN Cassegrain cone on the 64-m-diameter antenna. Air conditioning equipment to control the environment in upper modules and the Cassegrain cone was located in the lower module.

5.2 S-Band, 1966

The RF design of the original S-band feed system that was installed on the antenna was a physical scale of the 26-m antenna [2,3]. It consisted of the dual-mode [4] feed horn, a subreflector consisting of a 20-ft (6.090-m) hyperboloid together with a beam-shaping extension flange [5], a vertex plate in the central region [6], and a main paraboloid with $F/D = 0.4235$. The basic design philosophy for the subreflector was to (a) choose the largest subreflector possible, based on analysis of the blocking sidelobe level and (b) use the smallest horn-aperture-to-hyperboloid spacing that was structurally practical and did not further increase the blockage by feed-horn shadow on the main reflector (caused by the central rays from the subreflector). This design philosophy minimized forward spillover while maintaining a modest feed-horn size.

Potter [5] suggested an additional improvement in the subreflector design, involving the use of a flange that would both reduce forward spillover (less noise from interfering sources near the main beam) and rear spillover (less noise from the ground) while simultaneously increasing the aperture efficiency. The geometry of the beam-shaping flange is shown in Fig. 5-4. The forward spillover was reduced because of the larger extended angle, with consequent lower feed-horn pattern level. The rear spillover was reduced because the energy radiated from the flange near the edge of the main reflector was subtracted from the energy radiated from the hyperboloid, effectively steepening the slope at the edge of the main reflector and consequently reducing the rear spillover. Reduced forward and rear spillover were also aided by the increased size of the subreflector. A one-tenth scale model was built and tested, and the flange angle was experimentally determined to be 18.4 deg as a suitable compromise between aperture efficiency and low-noise performance.

A block diagram of the equipment used in the initial feed horn is shown in Fig. 5-5; the feed horn provided a gain of 61.47 ± 0.4 dB and a noise temperature at zenith of 27 K at 2.295 GHz. (The gain was measured using the high signal level (−100 dBw) received from the Surveyor 1 spacecraft, using a gain

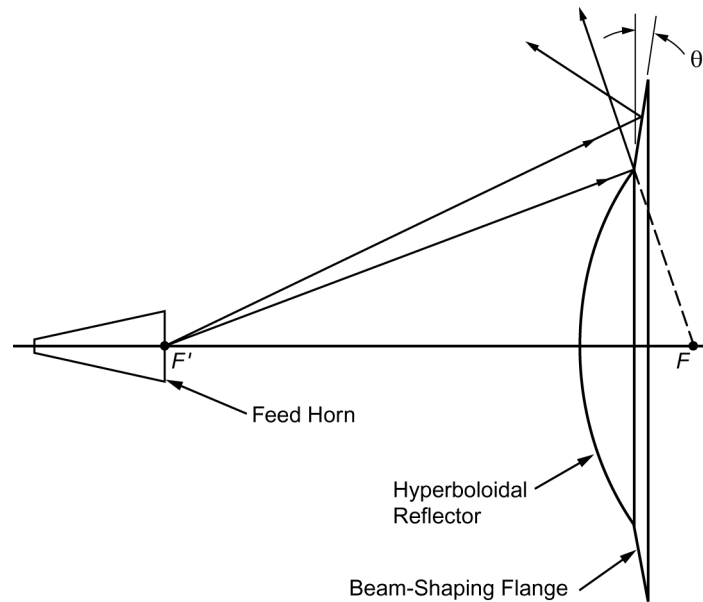


Fig. 5-4. Geometry of shaped-beam subreflector.

comparison method.) This feed system used a dual-mode horn, polarizer, and orthogonal-mode transducer.

Later, an experimental S-band feed system (called the ultracone) was designed as a minimum system-temperature, listen-only feed horn suitable for use on the Venus 26-m antenna (see Chapter 4) during the Mariner 5 Venus encounter in 1967. This feed horn was modified to include a diplexing capability and was installed on the Deep Space Station 14 (DSS-14) 64-m antenna in March 1968.

Based on the advanced capability demonstrated in terms of low total (zenith) operating temperatures of 17 and 28 K (listen-only and diplexed, respectively), a commitment was possible to support a high-data-rate (16.2 kb/s) experimental video data system experiment for the 1969 Mariner 6 and 7 project.

Further improvements in the feed-horn system were completed in time for the Mariner 6 and 7 Mars encounter video playback operation, which provided total (zenith) operating temperatures of 16 and 22 K, primarily a result of an improved diplexing filter. The 16-K system-noise temperature, in the listen-only mode, consisted of 9.6, 2.2, and 4.2 K for the antenna, dissipative loss, and preamplifier input noise contributions, respectively.

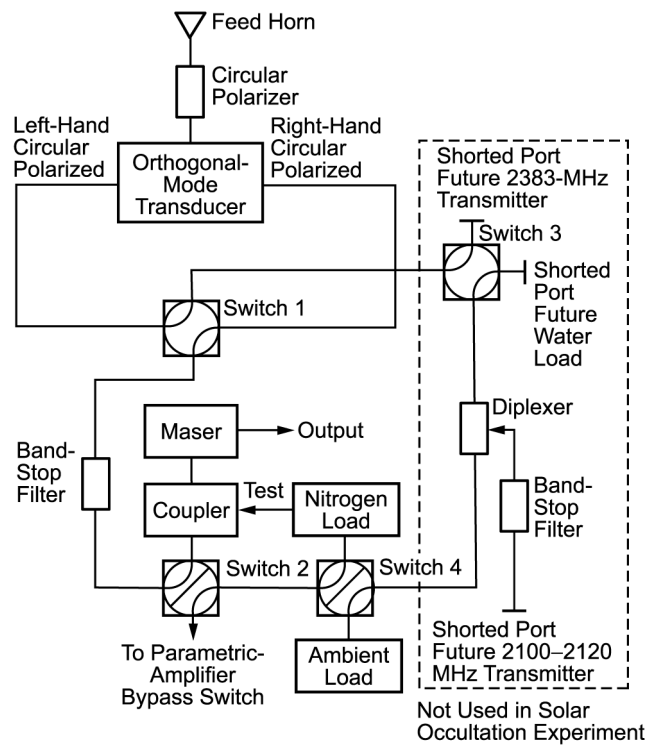


Fig. 5-5. Original feed-horn block diagram.

5.3 Performance at X-Band

Late in 1966, an X-band (8.448-GHz) Cassegrain experimental feed cone (XCE) was constructed. This feed cone was initially used for detailed evaluation of the 26-m Venus antenna [7]. In February 1968, it was used to evaluate the X-band performance of the 64-m antenna [8,9]. This new system gave the DSN the ability to clearly define surface tolerance. Previously, RF loss at S-band was sufficiently low as to make difficult an accurate RF measure of surface tolerance. The XCE cone contained a feed that was a scale model of the Venus radar feed (a dual-mode Potter horn), an X-band receive maser, and a total power radiometer. The subreflector flange, which was nominally 2λ wide at S-band, was considerably larger at X-band. Because of this, an analysis of the scattering from the Cassegrain system was performed using Rusch's scattering programs [10,11]. There was a slight pattern distortion due to the large wavelength flange, which degraded the system somewhat, but did not necessitate the removal of the flange.

The predicted value for the RF optics efficiency of the 64-m antenna fed with the XCE feed-horn system [8] was

$$\eta_0 = 0.629 \pm 0.024$$

where the surface tolerance quoted below in Section 5.3.1 is an estimated 1-sigma value, primarily due to quadripod blocking uncertainty.

5.3.1 Surface Tolerance

The RF surface comprised the 552 individual surface panels having factory-measured distortions with respect to their mounting legs. The distortions of the surface-panel mounting points were measured at the 45-deg elevation angle, and the gravity distortion as a function of elevation angle was computed using the STAIR structural computing program [12]. The gravity-load-deflection vectors as output from STAIR were evaluated by calculating one-half the RF path lengths of the residuals following best-fitting by a perfect paraboloid, assuming a new focal length as a best-fitting parameter.

Best-fit paraboloid translations, x-axis rotations, quadripod, and subreflector deflections were also computed. An equivalent root-mean-square (rms) distortion was compiled from a power sum of the key components (each expressed in rms millimeters): (a) the lateral and (b) axial misalignments occurring at the paraboloid focus, (c) the paraboloid structure gravity distortion, and (d) the component due to panel manufacturing error.

The errors associated with each of these components were taken in two ways: one allowed for axial focusing of the subreflector and a second constrained the system to a fixed-focus mode. The fixed-focus mode was adequate at S-band, but the axial focusing mode was required at X-band. The measured surface errors at 45 deg are shown in Table 5-1, and the rms surface tolerance as a function of elevation is shown in Fig. 5-6 compared to an RF-derived mea-

Table 5-1. Measured surface distortion of the 64-m antenna at a 45-deg elevation angle.

Error Source	Error (rms, in mm)
Surface-panel setting	0.48
Primary surface-panel manufacturing	0.89
Subreflector manufacturing	0.69
Total RF half-path-length error	1.22

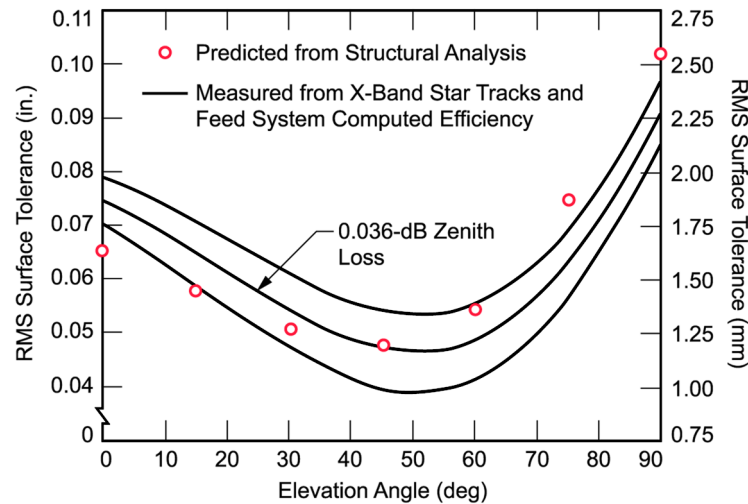


Fig. 5-6. Surface tolerance as a function of elevation angle, 8.448 GHz.

surement of the rms. The gain measurement was converted to rms, using the standard Ruze [13] technique.

5.3.2 Measured X-Band Performance

Operating on the ground in a checkout mode, the XCE feed horn, pointing to the zenith, exhibited a 33.5-K total operating temperature. The individual noise sources were thought to be $T_M = 13.7$ K at the maser input, $T_L = 13.2$ K, $T_F = 0.1$ K at the maser input, and $T_A = 6.8$ K at the horn aperture, where T_M , T_L , T_F , and T_A are the maser, the loss, the follow-up receiver, and the antenna temperature contributions, respectively. When operated on the 64-m antenna, an additional 3.3-K noise temperature at zenith was observed. This additional noise was caused primarily from feed spillover and quadripod scatter towards the warm earth. A total X-band Cassegrain antenna temperature defined at the feed-horn aperture of 10.1 K appears a reasonable estimate. Comparable S-band values were an incremental 3.6 K and a total of 9.3 K.

The 64-m antenna was equipped with subreflector axial drives and, as indicated earlier, axial focusing as a function of elevation angle was used. The RF data was found to be in good agreement with the structural predictions and was used throughout the X-band evaluation.

The peak measured system gain and efficiency were 72.3 dB and 52 percent, respectively. The inaccuracy of radio star flux at these frequencies yields an error in the measurement of ± 0.8 dB. Accepting a system surface tolerance

maximum of 1.65-mm rms as applicable over a very wide range of elevation angles, the predicted gain limit should have occurred in the 2-cm band.

5.4 Tricone Multiple Cassegrain Feed System

Several major modifications were made during the early years of operating the 64-m antenna, to improve the capability of the antenna. The most significant of these was to provide a method for rapidly changing the RF feed horns. The unicone system not only required valuable operating time to change cones, but it also presented risks of possible damage during handling procedures. The solution was to replace the standard feed-horn support structure with a structure capable of supporting three fixed feed horns clustered about the antenna axis and pointed toward the antenna subreflector. By suitable choice of Cassegrain geometry, a focal ring was realized, with a given cone brought into focus by rotating an asymmetrically truncated subreflector about its symmetric axis and pointing it toward the feed.

The principle of the focal ring is illustrated in Fig. 5-7. In a symmetric Cassegrain system [Fig. 5-7(a)], the feed is located on the centerline of the paraboloid at one of the two foci (point B) of a hyperboloid, and the other focal point (A) is located at the focal point of the paraboloid. The line AB thus defines the axis of the hyperboloid, and the hyperboloid transforms a spherical wave from the feed-phase center, B, into a spherical wave from the vertical focus at point A. For the asymmetric case [Fig. 5-7(b)] the axis (line AB) is rotated through an angle β around point A. Since A is also located at the paraboloid focus, the paraboloid is illuminated by a spherical wave from its focus, and no boresight error or aperture phase error is introduced by the tricone geometry. However, since the geometry is asymmetric with respect to the center line,

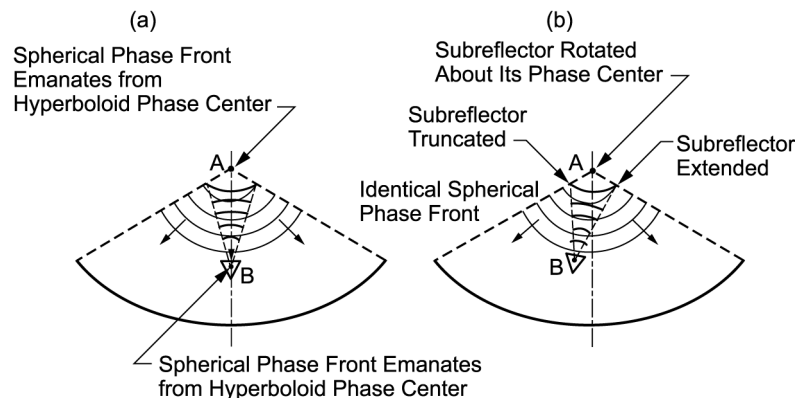


Fig. 5-7. Comparison of symmetric and asymmetric feed systems.

there is an amplitude taper, which is controlled by two methods. The first is by truncating the hyperboloid asymmetrically so that the subtended half-angle at the edge as seen from the paraboloid focus A is uniformly 60 deg—the same value utilized in the unicone design. This asymmetric truncation is necessary to control the rear spillover. The second is by rotating the feed about its phase center B so that the axis of radiation intersects the geometric center of the hyperboloid's area.

The geometry of the tricone is further illustrated in Fig. 5-8. The feed-illumination angle is sufficiently close to the unicone values so that the same feed design can be used. For the 64-m geometry, the rotation angle β was 4.517 deg, and the feed phase center was 42.523 in. (1.08 m) from the center axis. The concept of the subreflector flange was maintained in the asymmetric design. Figure 5-9 shows the tricone installed on the 64-m antenna.

Rotation of the subreflector about its axis of symmetry was achieved by means of a large bearing within the torus assembly. Five rotational positions were provided by an indexing pin system. Three of these positions corresponded to the centers of the tops of the three feed horns; this provision was made in anticipation of using multiple high-frequency feed horns.

5.4.1 Radio Frequency Performance

During the design of the tricone system, a series of scale model tests of the subreflector and horn assembly was made, and additional analysis was performed to verify the expected performance. Analysis based upon both the calculated and the scale-model-measured scatter patterns from the subreflector showed a gain loss of 0.06 to 0.09 dB over the unicone, with the loss almost

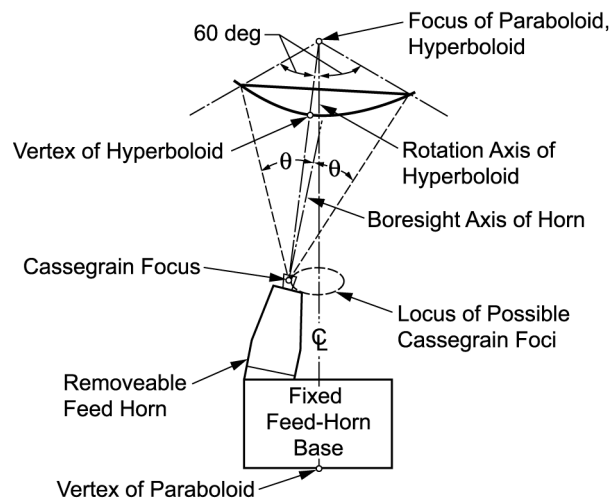


Fig. 5-8. Tricone geometry.



Fig. 5-9. Tricone installed on the 64-m antenna.

entirely due to the increased central blockage in the tricone configuration rather than to a difference in illumination function. In fact, the portion due to difference in illumination function was only 0.008 dB.

After the successful completion of the tricone installation, verification tests of S- and X-band performance were conducted. At S-band, in order to perform a direct test of the tricone effect on performance, the same feed horn was utilized as in prior unicone tests. Contrary to the predicted small degradation, the tricone gain was higher than the unicone gain by 0.1 dB. This discrepancy has never been fully explained. At X-band, a larger improvement, 0.5 dB, was measured. However, in this case, a different feed horn was utilized that had 0.1-dB less insertion loss. Thus, the improvement of the tricone was only 0.4 dB. This discrepancy has also not been fully explained but is thought to be due to an improved surface tolerance caused by the fact that the reflector panels were originally aligned for an estimated central weight that more closely resembled that of the tricone rather than that of the unicone.

5.4.2 New Wideband Feed Horns

Around the same time as the tricone geometry modification, a new wideband feed horn was developed [14] that was designed around the principles described by Minnett [15]. As previously described, the Potter dual-mode horn [4] achieved equal beamwidths, suppressed sidelobes, and identical E- and H-plane phase centers by the use of multiple waveguide modes in the feed horn. However, Potter's technique of generating and phasing the modes had the disadvantage of being relatively narrowband (about 9 percent). As described by Minnett, the use of a corrugated waveguide structure achieves the same results with a much wider bandwidth (28 percent in the development model). A feed horn was designed with equal E- and H-plane beamwidths, sidelobes more than 30-dB below the peak of the beam, and a voltage standing-wave ratio (VSWR) of less than 1.1 over two frequency bands of 7.767–7.801 GHz and 8.429–8.466 GHz and at two distinct frequencies of 7.84 and 8.79 GHz. This bandwidth would be sufficient to cover the S-band uplink and downlink frequencies as well as projected experimental frequencies. The use of such a horn at S-band increased the gain of the DSN antennas by more than 1 dB at the uplink frequency. There was no appreciable change at the downlink frequencies since the prior dual-mode horns were already optimized for them. Physically, the developmental mode horn had a 7.077-in. (17.98-cm)-diameter aperture, a 6.2542-deg half-flare angle, and an input section diameter of 1.369 in. (3.48 cm). A single, large circumferential slot was used for impedance matching. The remaining corrugations were the wideband mode generators, which continued for the entire length of the horn.

The developmental feed horn was accepted as the JPL standard 22-dB horn, and all subsequent 22-dB horns have utilized this design, even though better methods of matching corrugated horns have been developed. The S-band horn was a scale of 8.448/2.295 times the X-band horn. Both the S-band and X-band tricones were fitted with wideband corrugated horns.

5.4.3 Dual-Hybrid-Mode Feed Horn

Prior to 1970, most DSN feeds were based upon the use of two waveguide modes propagating within a smooth conical waveguide—the so-called Potter horn [4]. Due to the length of high-gain feed horns, the proper phase synchronism at the feed-horn aperture between the waveguide modes was achieved only over a restricted bandwidth (5 to 10 percent). In the DSN, this had previously meant that enhanced horn performance was achieved at the downlink band while the transmit performance was equal to or less than single-waveguide-mode feed horns.

Work to realize better feed-horn performance (pattern shaping) was only partially successful at that time. Three- and four-mode smooth conical

waveguide feed horns were devised by Ludwig [16]. However, the difficulties of controlling mode amplitudes and phases for specific use on DSN antennas were great. It was concluded that only marginal performance was practically available beyond the two-mode feed horns.

By 1970, the principles described by Minnett were applied to feeds for the DSN, with excellent results. Minnett's type of feed horn is based upon one hybrid mode (transverse-electric [TE] and transverse-magnetic [TM] component) conducted along a corrugated conical waveguide. This lowest-order hybrid mode, HE_{11} , used within a waveguide, maintains itself nearly distortion free over a very broad bandwidth, since no phase asynchronism problems arise. It is then possible to provide superior performance over both the uplink and downlink bands.

In a manner analogous to adding individual TE and TM modes within a smooth-surface conical waveguide, it is possible to add hybrid modes within a corrugated waveguide. By so doing, it is possible to approximate a radiation pattern that puts additional energy near the outer edge of the parabolic reflector, approximating a more uniform aperture illumination taper and, hence, yielding a higher overall gain.

Figure 5-10 shows the throat region of the 8.45-GHz horn described in the preceding paragraph [17]. The TE_{11} input waveguide remained the same as in previous X-band horns. The abrupt step, in addition to exciting the HE_{12} mode, also played a major role in controlling the amplitude ratio between the two hybrid modes. The horn flare angle was the same as for existing (at the time) JPL feed horns. The aperture size of 12.563 in. (31.91 cm) was approximately optimum for the 14.784-deg half-aperture angle of the 64-m antenna with tri-cone feed subreflector. By experiment, the phase center was found to be 7.88 in. (20 cm) inside the aperture.

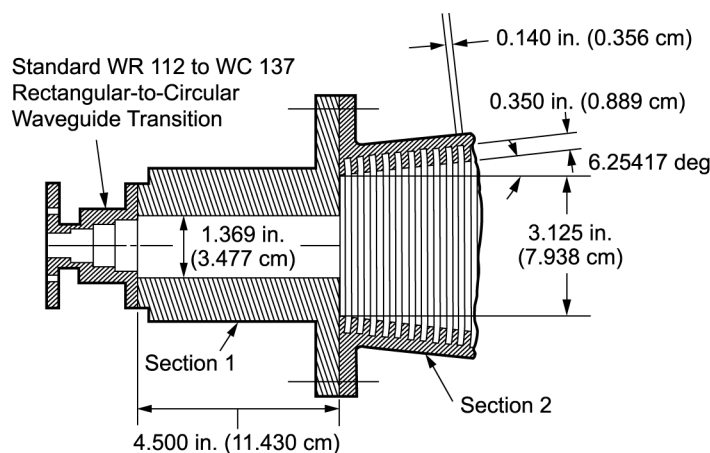


Fig. 5-10. Throat region of dual-hybrid-mode feed horn.

Figure 5-11 shows the feed-horn amplitude patterns of the single-hybrid and dual-hybrid-mode feed horns at 8.45 GHz, and Fig. 5-12 the E- and H-plane amplitude patterns scattered from the symmetric equivalent subreflector of the existing 64-m tricone feed system. The more uniform amplitude illumination produced by the dual-hybrid feed horn was clear. Table 5-2 gives the results of efficiency calculations on the two patterns of Fig. 5-12. For the symmetric case, a performance increase of 0.36 dB was available. It was estimated that a loss of 0.07 dB would occur if the feed were used in the 64-m asymmetric system, due to energy converted into the $m \neq 1$ modes. The net available improvement was, therefore, +0.29 dB.

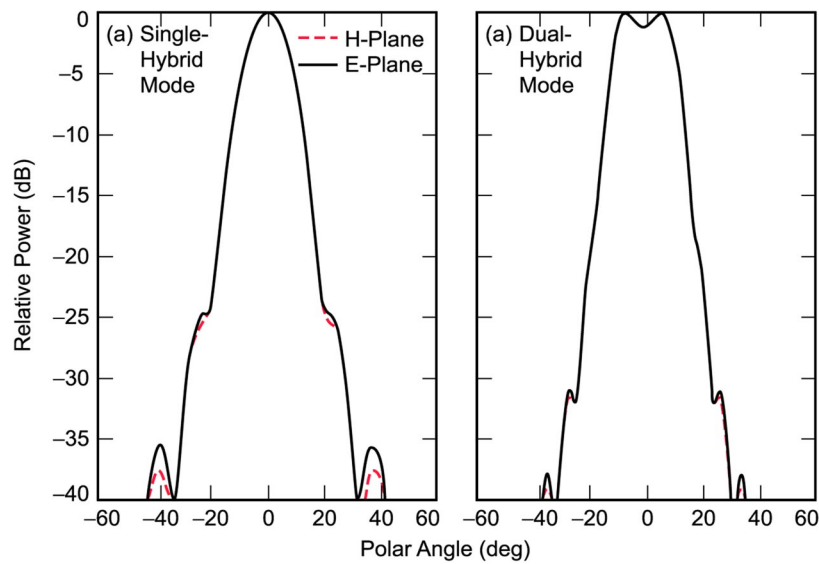


Fig. 5-11. Feed-horn amplitude patterns (8.45 GHz): (a) single-hybrid-mode feed and (b) dual-hybrid-mode feed.

Table 5-2. Subreflector scattered pattern efficiencies, tricone symmetric equivalent subreflector (8.45 GHz).

Efficiency Terms	Single-Hybrid-Mode Feed	Dual Hybrid-Mode Feed	Dual-Hybrid-Mode Improvement (dB)
Spillover	0.9447	0.9529	+0.037
Illumination	0.8474	0.9008	+0.266
Cross-polarization	0.9999	0.9999	0.000
Phase	0.9718	0.9670	-0.021
Blocking	0.9441	0.9616	+0.080
Total	0.7344	0.7981	+0.361

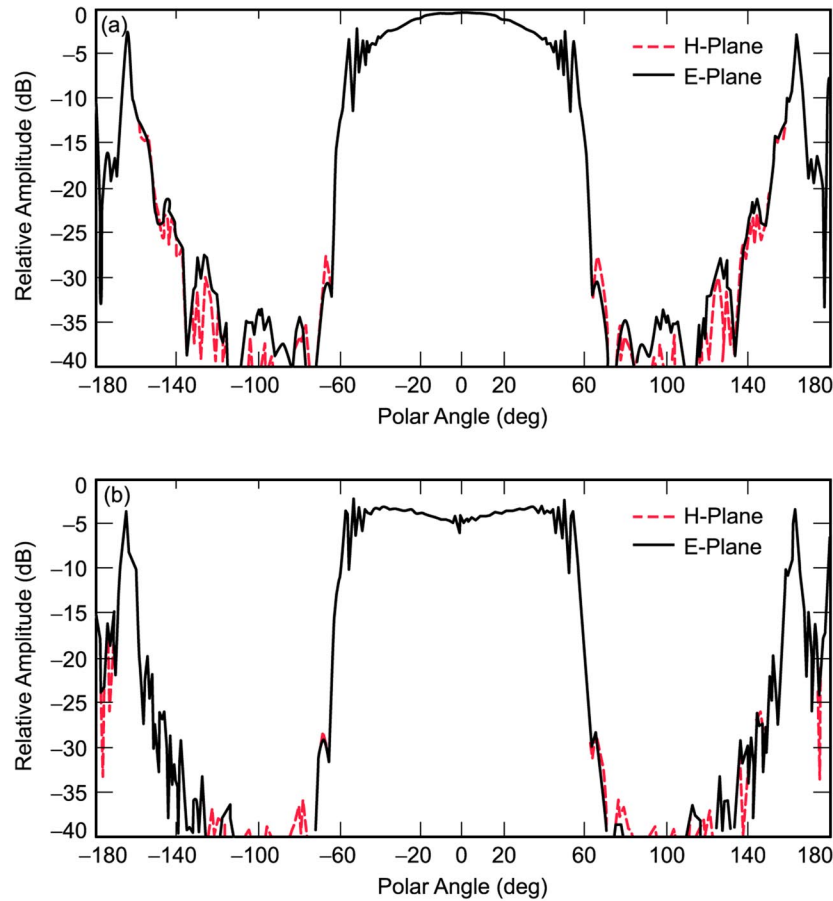


Fig. 5-12. Symmetric subreflector amplitude patterns: (a) single-hybrid-mode feed and (b) dual-hybrid-mode feed.

The X-band feed-horn assembly [18] on the DSN 64-m antennas originally provided the capability for selectable right-hand circular polarization (RCP) or left-hand circular polarization (LCP) [19]. Designed to work with a signal traveling-wave maser (TWM), the X-band receive-only (XRO) cone assembly was then upgraded to include dual TWMs [19]. As part of that reconfiguration, provision was made for a new feed assembly, the Mod III XRO, that would include two basic improvements over the feeds that had been in use since early 1977. The first improvement was the development of an orthogonal-mode transducer that permits simultaneous reception of two different polarizations. The second improvement was the incorporation of a dual-hybrid-mode feed horn to increase the antenna gain.

The new feed assembly is shown in Fig. 5-13. It was designed for mounting within the XRO cone assembly on the same circular mounting plate as the previous feeds (Mod I and Mod II), so that replacement in the field was expedited [20,21]. Each output arm of the orthogonal-mode transducer has its own waveguide switch for TWM calibration.

The 64-m antenna X-band system at DSS-14 was evaluated to determine the performance with the new dual-hybrid-mode feed. The peak system efficiency increased from 42.0 to 45.6 percent, resulting in a 0.36-dB increase in antenna gain (see Fig. 5-14). The new measured gain was 71.6 dB. Antenna pointing, beamwidth, optimum subreflector focusing, and operating system temperature were unchanged from the previous feed. Some evidence of antenna aging was apparent (from the 1973 measurements reported earlier) both in peak gain and in the pointing angle at which the peak occurs. Further data can be found in [22].

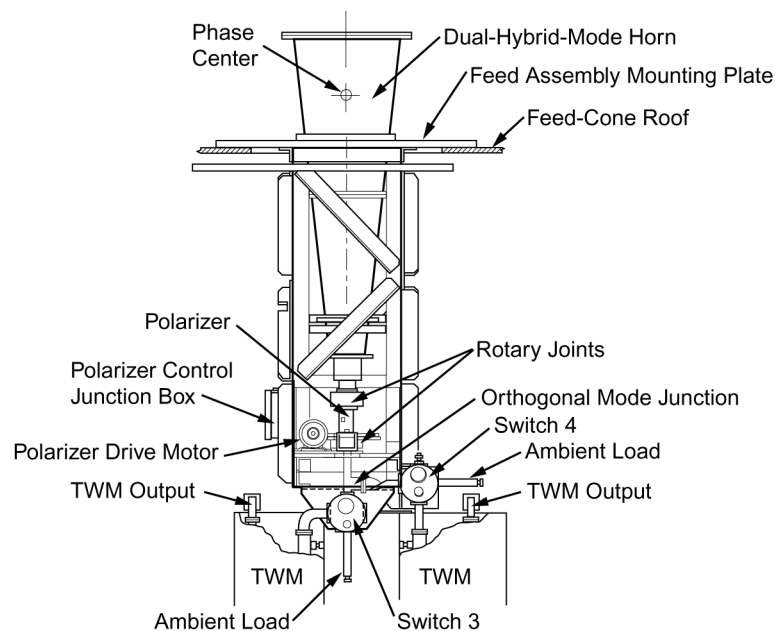


Fig. 5-13. Mod III XRO feed assembly.

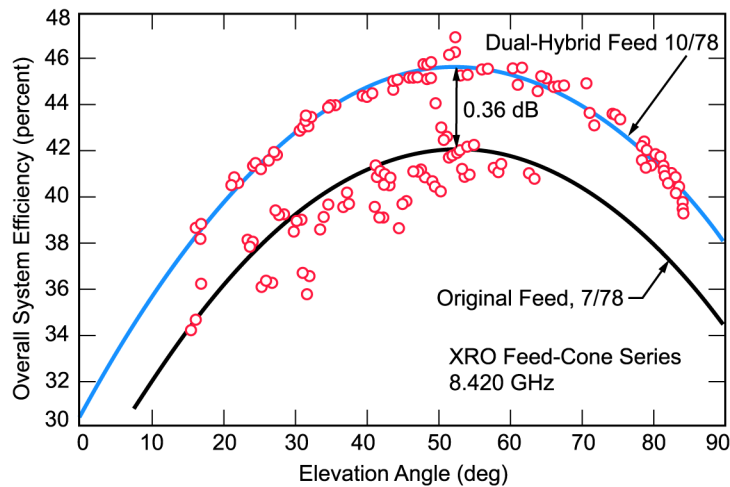


Fig. 5-14. Antenna system efficiency at X-band with dual-hybrid-mode feed horn.

5.5 Reflex–Dichroic Feed System

The tricone geometry was adequate to support single-band communication, but was unable to handle simultaneous multifrequency operations. This need arose in support of the Mariner 1973 X-band experiment, where a system was required to provide simultaneous low-noise reception at S- and X-bands and high-power transmission at S-band. Since S-band was still the primary frequency, the emphasis of the design was for minimal degradation at the S-band receive frequency.

A cross-sectional view of the reflex feed system [23,24] is shown in Fig. 5-15. The feed system made simultaneous use of both an X- and S-band feed horn. By using two reflectors—one an ellipse and the second a planar dichroic reflective at S-band—the effective S-band phase center was translated from its normal position in the S-band feed horn to a new point that nearly coincided with the X-band feed-horn phase center. This translation occurred as follows: since the ellipsoidal reflector was small in terms of wavelengths, the radiated energy focused short of the ellipsoid F_2 geometric focus, point C in Fig. 5-15.

The energy was then redirected by the planar reflector to the antenna subreflector. By the image principle, this redirected energy appeared to emanate from the point F_x , which is both the far-field phase center of the X-band feed horn and the subreflector focal point when it is aligned with the X-band feed-

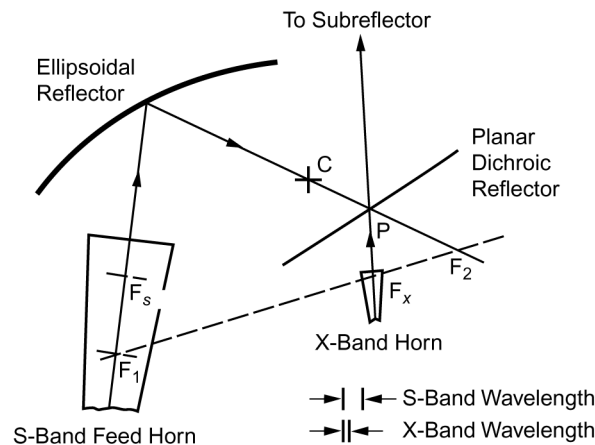


Fig. 5-15. Reflex-dichroic feed system.

horn position. To permit simultaneous X-band operation, the central region of the planar reflector was a thick plate filled with circular holes designed to make the reflector essentially transparent to X-band while still reflective to S-band.

The basic performance of the reflex-dichroic feed system is given in [25], from which the following explanation is abstracted.

Because of the asymmetric geometry, the S-band reflex feed patterns did not exhibit as high a level of symmetry as the corrugated waveguide feed horn taken alone. Spherical-wave techniques were used [26–28], to predict overall S-band performance. Because this feed design was based on a series of computer programs, it was considered necessary to experimentally check the predictions. A 1/7 scale-model program produced measured patterns in both polarizations essentially identical to those shown in Fig. 5-16. Also shown in Fig. 5-16 are the predicted scattered patterns of both the feed-horn ellipsoidal reflector, referenced to F_s' , and the horn ellipsoid and flat plate (simulating an opaque dichroic filter) taken together, referenced to F_x .

Table 5-3 summarizes the predicted gain performance of the S-band reflex feed and compares that with previous tricone performance, itself a slightly asymmetric system. Table 5-3 illustrates the familiar trade-off in forward spillover and amplitude illumination loss, which is a function of feed-horn gain. In this case, the reduced forward spillover was a result of slightly higher gain for the horn/ellipsoid/flat-plate patterns than for the horn alone. Table 5-3 also shows the major penalty of asymmetric systems: radiated energy not contributing to forward antenna gain ($m \neq 1$) and resultant cross-polarization. In summary, the reflex system was expected to degrade S-band gain performance less than 0.06 dB, and negligibly impact the S-band noise temperature.

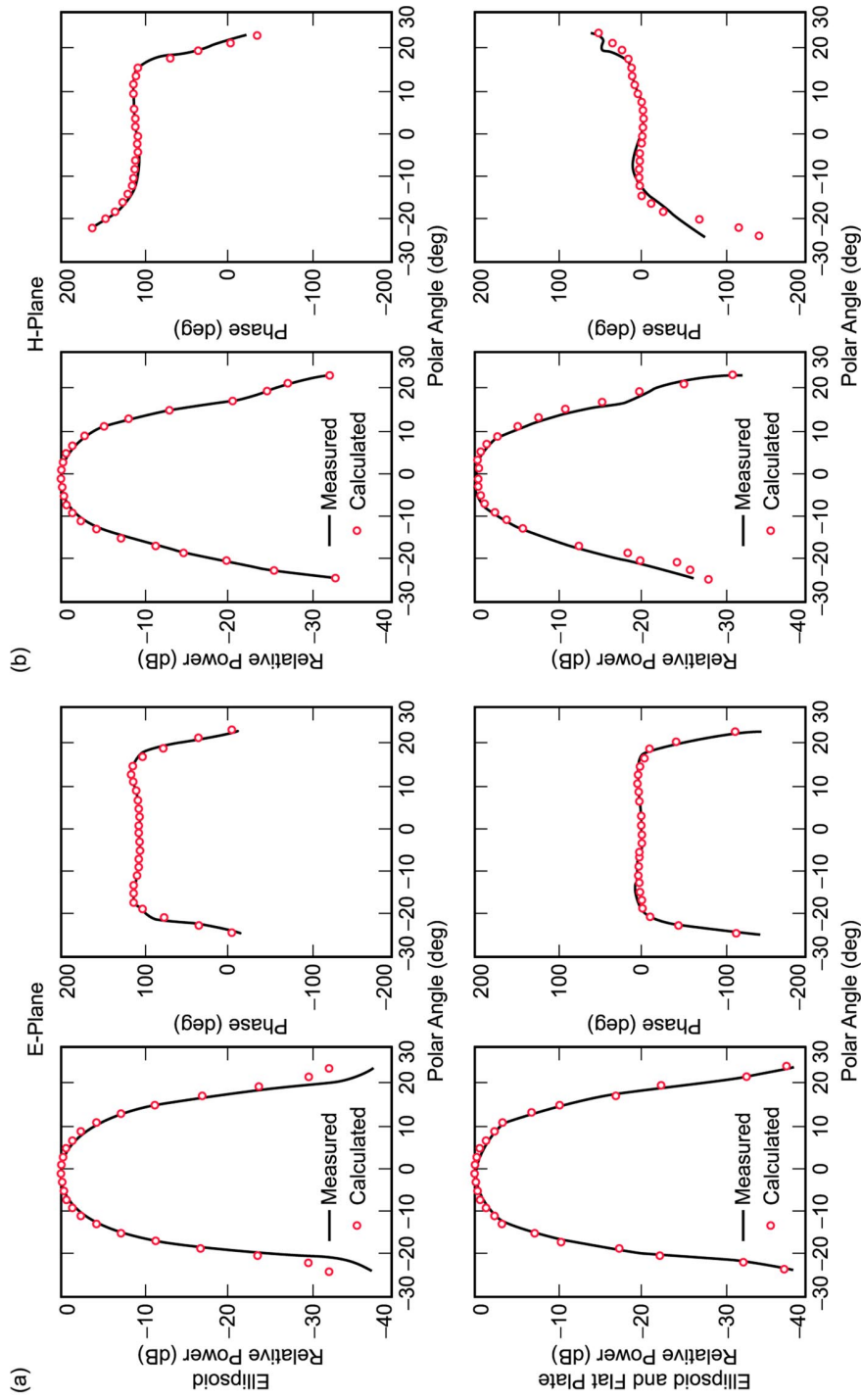


Fig. 5-16. Calculated and measured low-band patterns: (a) E-plane and (b) H-plane.

Table 5-3. Predicted S-band gain performance with tricone and reflex-dichroic feeds.

Gain Factors	Predicted Gain (dB)		Notes
	Tricone	Reflex-Dichroic	
Forward spillover	-0.247	-0.133	None
Rear spillover	-0.011	-0.010	None
Amplitude illumination	-0.747	-0.840	None
Phase illumination	-0.088	-0.070	None
Cross-polarization	-0.001	-0.005	None
$m \neq 1$ energy	-0.009	-0.089	Due to asymmetric geometry
Central blockage	-0.262	-0.260	None
Quadripod blockage	-0.580	-0.580	None
Surface measurement	-0.093	-0.093	Main and subreflector (rms = 1.52 mm)
Surface tolerance	0	-0.010	Ellipsoid (rms = 0.51 mm)
Surface tolerance	0	Negligible	Dichroic
Resistivity	0	-0.003	None
Total	-2.038	-2.093	None

For the X-band dichroic plate, preliminary designs were based on discussions with and previous work by individuals at The Ohio State University. That work was extended for circular polarization [29]. These filters were physically ultrathin (0.4 mm) and perforated with an array of reactively loaded close spaced slots. For this application, the original filters were found inadequate in the dissipation loss sense, providing 0.3-dB loss at X-band for aluminum construction. It should be noted that 0.3 dB of ambient-temperature dissipation, when added ahead of a 21-K total operating-noise-temperature receive system, results in a gain-over-temperature (G/T) degradation of 3 dB due to doubling of the temperature term.

Intermediate filter designs increased bandwidth with attendant lower dissipation losses (2 to 4 K) and thicker construction (3 mm). These intermediate designs also suffered from mechanical tolerance sensitivity problems as well as probable severe degradation due to paint, dirt, and water droplet accumulation. Finally, due to the aspect ratio (3-mm thickness, 1-m diameter), and the geometrical constraints, a difficult thermal distortion problem was identified. When illuminated with 400-kW S-band, with a beam diameter of approxi-

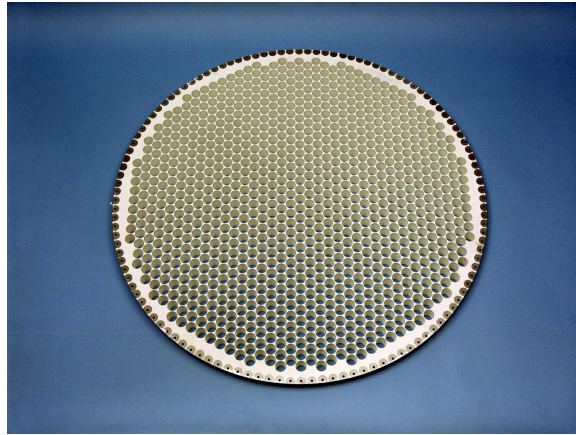


Fig. 5-17. Half-wave-thick dichroic filter.

mately 40 cm, the thin filters invariably heated and became bowed relative to S-band flatness requirements.

An excellent alternative to the thin, thermal-dependent-type dichroic filters was proposed and developed by Potter [30]. The solution was to obtain resonance by the simple means of a half-wave-thick array of dominant-mode cylindrical waveguide apertures. At X-band, this construction is 1.42-in. (3.6-cm) thick, with a calculated dissipation loss of 0.012 dB, using aluminum (Fig. 5-17). Measurements showed an operating system-noise-temperature increase of 1.2 K (0.01 dB) due to dissipation, with virtually no X-band pattern degradation. Bandwidth was approximately 100 MHz for the specific tilt angle and horn beamwidth (angular scan) employed.

Because the geometry shown in Fig. 5-15 tilts the dichroic filter at 30 deg off normal to the X-band feed-horn boresight, the E- and H-plane dichroic resonant frequencies were slightly split. Use of circular polarization resulted in different transmission phase shifts for orthogonal waves transversing the filter. The differential phase shift resulted in an on-axis X-band ellipticity of 1.8 dB, which, accepting a perfectly circularly polarized antenna at the other end of a link, produced an additional 0.04-dB transmission loss. Another result of differential resonant frequencies for the tilted array was an approximate -18-dB reflection. This had two effects: an additional 0.04-dB reflection loss and a slowly varying noise-temperature term for the complete antenna, due to scatter, which is a function of elevation angle. The magnitude of this additional noise was 0.4 to 1.2 K.

The total gain degradation at X-band was, therefore, 0.10 dB for a link employing circular polarization. The total noise-temperature degradation was 1.6 to 2.4 K. Accepting 2.0 K as an average, and referenced to a base operating

noise temperature of 21 K, 0.4 dB was lost to noise, for a total G/T reduction of 0.5 dB.

Tests were conducted on the 64-m antenna to include measurement of G/T at both bands; boresight coincidence or beam coaxiality; and high-power transmission, at frequencies of 2.295, 8.415, and 2.115 GHz, respectively. Table 5-4 summarizes the measured performance of the full-scale prototype dual-band feed horn as installed at Goldstone, California, in January 1973.

Table 5-4. Predicted and measured performance summary, reflex–dichroic feed.

Band and Gain or Temperature	Predicted	Measured	Notes
S-band gain	−0.055 dB	−0.03 dB	Measurement includes 0.045-dB pointing loss
S-band temperature			
Above 30-deg elevation angle	0.0 K	0.0 K	
Below 30-deg elevation angle	0.0 K	2.0 K	Improvement
X-band gain	−0.10 dB	−0.10 dB	Circular polarization
	−0.06 dB	−0.06 dB	Random polarization
X-band temperature	+1.6 to 2.4 K	+1.5 to 2.3 K	None
			None

Measured S-band gain indicated improved performance (+0.01 dB) when pointing on the S-band beam peak. When allowance for a 0.04-dB pointing loss was made (discussed below), S-band gain performance difference between reflex and non-reflex modes (0.03 dB) was difficult to distinguish. Because of the reduced forward spillover and the tricone geometry, S-band noise-temperature performance was improved. However, most of this improvement was due to relative feed-horn positions upon the tricone with respect to the ground and was not attributed to the new feed. This was so because the S-band radiation, in the reflex mode, effectively emanated from F_x rather than F_s . X-band measured performance was in perfect agreement with predictions. The standard deviations in the gain difference determinations were approximately 0.02 dB and 0.10 dB for S- and X-bands, respectively. No deleterious thermal effects were observed with use of full uplink power.

Figure 5-18 is a view, facing the parabolic reflector relative to local vertical, of the RF beam positions in space. Four beams are shown: the singular S- and X-band nonreflex beams (subreflector individually focused and dual-band reflectors stowed) and the simultaneous reflex beams (subreflector

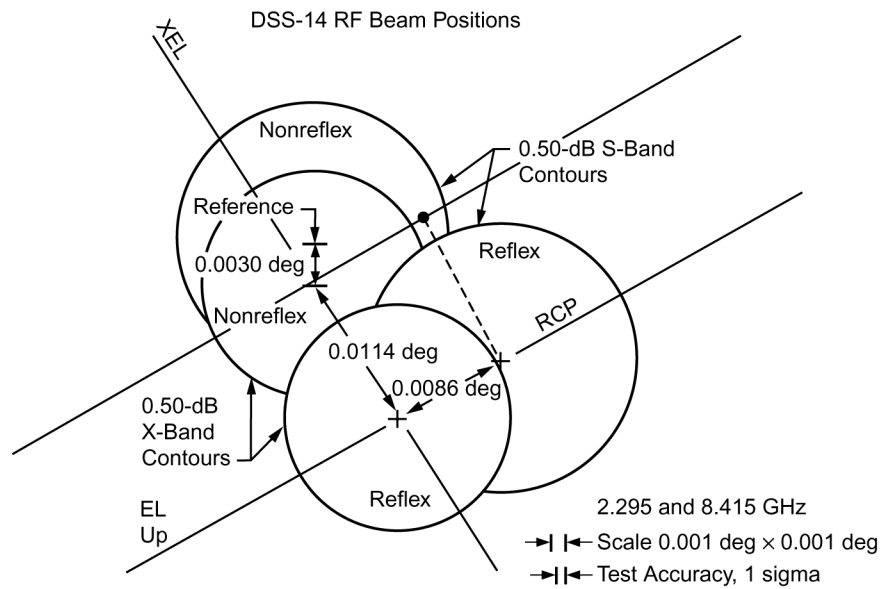


Fig. 5-18. RF beam positions.

focused to F_x and dual-band reflectors functional). Several observations are worth noting. The singular S- and X-band beams were offset 0.003 deg, which is typical of DSN attained accuracy in feed-horn placement within the feed horns (± 6 mm) and tricone subreflector repeatability. Use of the dichroic reflector produced a noticeably lower X-band reflex beam (0.011 deg); this resulted from refraction through the relatively thick dichroic plate. The 30- to 60-deg characteristic seen in Fig. 5-18 was traceable to the tricone geometry with respect to local vertical. Upon first installation, the S-band reflex beam was found to be displaced 0.009 deg to the right of the nonreflex beam. This effect resulted from use of circular polarization in the presence of the asymmetric geometry-induced cross-polarization mentioned above. Although not verified, it was predicted that use of the opposite-hand circular polarization would produce an S-band reflex-beam peak displaced an equal amount to the left of the nonreflex beam.

Figure 5-19 shows the full-scale reflex–dichroic feed on the 64-m antenna.

5.6 L-Band

In support of several international space exploration projects—the French/Soviet Vega mission to Venus (June 1985) and comet Halley flybys (March



Fig. 5-19. Reflex–dichroic feed on the 64-m antenna.

1986)—JPL was asked in late 1983 to modify the DSN to receive L-band (1.668-GHz) telemetry used by the Soviet space program.

An extensive description of the Venus Balloon Project and L-band system requirements is given in [31]. The following requirements affected the design of the microwave system:

- Antennas must receive $1.668 \text{ GHz} \pm 5 \text{ MHz}$
- Antenna gain must be at least 58 dBi, or 50 percent efficiency on a 64-m antenna
- System-noise temperature (T_{op}) must be $<35 \text{ K}$ at zenith.

5.6.1 Design Approach

The required 58-dBi gain precluded the use of all DSN antennas except the three 64-m antennas. Since there was insufficient room for the feed horn in any of the existing feed cones, the solution was to suspend the feed horn in the area between the X-band receive-only (XRO) and the host-country feed cone (Fig. 5-20). The feed horn was cantilevered on a bracket bolted to the top of the XRO feed cone. As weight was then a critical concern, a sheet metal smooth-wall dual-mode horn 3.4 m long, with a 0.97-m aperture, was designed to be a light, low-loss, but narrowband (approximately $\pm 40\text{-MHz}$) solution with the illumination efficiency necessary to meet system requirements.

Due to the large aperture of the L-band feed horn, the phase center of the L-band feed lies some 60 cm (3.4 wavelengths) radially outward from the focus ring, which produces a small scan loss in beam-peak gain and beam-pointing

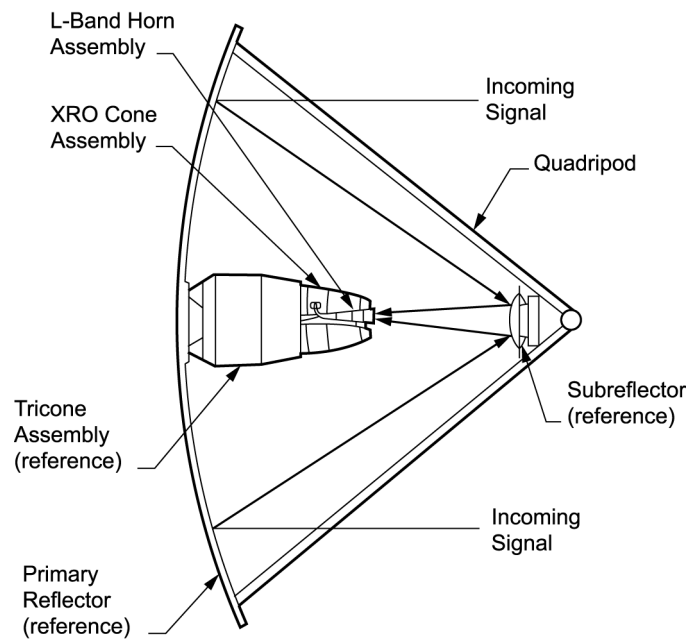


Fig. 5-20. L-band feed-horn antenna position.

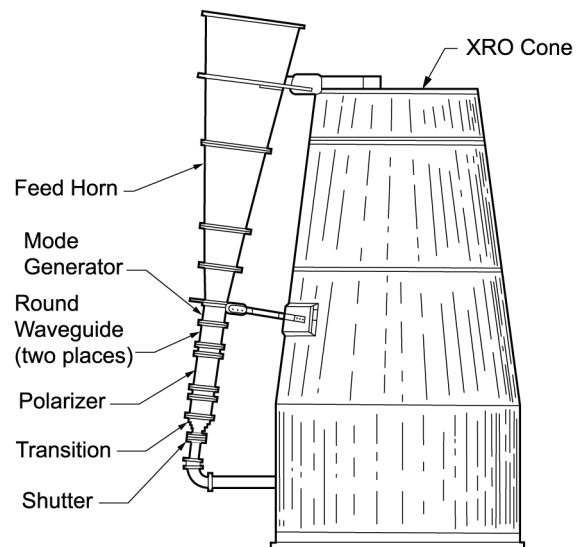


Fig. 5-21. L-band feed-horn geometry.

squint. Figure 5-21 shows the basic horn and antenna geometry used on the three 64-m antennas.

A narrowband ($1.690 \text{ GHz} \pm 50 \text{ MHz}$) quarter-wave plate polarizer was used to meet the circular polarization requirement. Spare DSN WR 430 waveguide components and a WR 430 switch completed the microwave feed system.

Two completely redundant, cryogenically cooled (physically cooled to 14 K) L-band field-effect-transistor (FET) low-noise amplifiers (LNAs) provide the necessary preamplification. The FET LNAs were designed with 38 dB of gain and a usable bandwidth of about 200 MHz. A bandpass filter in front of the amplifiers is used to limit the bandwidth response of the FET LNA to about 100 MHz ($1.668 \text{ GHz} \pm 50 \text{ MHz}$). This was done to prevent out-of-band noise (at 2.1 GHz) from the S-band transmitters of co-situated antennas in Spain and Australia and to prevent known radio frequency interference (RFI) threats from saturating the preamplifiers. (A signal level approaching -40 dBm may be enough to saturate these FETs.)

An L-band to S-band upconverter was used to convert the output of the L-band FETs to S-band. This allowed use of all station S-band receiver equipment necessary to meet Vega telemetry-processing requirements. The upconverter further limits the bandwidth of the L-band system to 10 MHz, fixing the total bandwidth of the overall L-band receive system at $1.668 \text{ GHz} \pm 5 \text{ MHz}$.

5.6.2 Performance Predictions and Measurements

The complete cooled FET system, with horn, polarizer, and waveguide, was assembled and tested to determine the microwave temperature contribution to the overall system T_{op} . The temperature contribution was determined to be approximately 10 K for the hardware and 14 K for the L-band FET LNA.

The measured values for gain, T_{op} , and scan offset on the three 64-m antennas are shown in Table 5-5. The T_{op} values were obtained using the Y-factor method. The predicted noise-temperature component values at zenith, given in kelvins, are shown in Table 5-6.

Table 5-5. Calculated and measured L-band microwave system efficiency, T_{op} , and scan offset.

Source	Efficiency at Approximately 45 deg of Elevation [percent (gain, dBi)]	T_{op} (K)	Scan Offset (deg)
Calculated (PO)	57 (58.5)	33	0.260
Measured at DSS-14	51 (58.2)	33	0.260
Measured at DSS-43	52 (58.2)	36	0.260
Measured at DSS-63	55 (58.4)	34	0.260

Table 5-6. Predicted noise temperature at zenith.

Parameter	Value (K)
Antenna temperature	8.5 (cosmic plus sky plus spillover)
Feed components	10.0
FET LNA	14.0
Receiver follow-on contribution	1.0
Total	33.5

A PO analysis predicted a scan offset angle of 0.26 deg, a half-power beamwidth of 0.19 ± 0.01 deg, with a slightly elliptically shaped beam (0.01-deg difference), and a peak gain of 59.46 dBi, or 70.6 percent efficiency. Additional antenna losses not included in the PO calculation, expressed in decibels and shown in Table 5-7, must be subtracted from the PO result.

Adding all losses, the PO-based prediction was that the scan axis gain peak should be 58.5 dBi for an efficiency of 57 percent. This is compatible with the measured data. The lower efficiency at DSS-14 may be due to saturation by RFI as these measurements were made before the full extent of FET saturation by RFI was understood. Some gain nonlinearity caused by saturation may account for the lower efficiencies. Further details on design and performance may be found in [32], along with a block diagram of the L-band receive-only system.

5.6.3 L-Band System Modifications

The L-band system successfully supported the French/Soviet Vega mission to Venus as well as the comet Halley flybys. The 64-m antennas were upgraded to 70-m, and the L-band system was modified to include a C-band transmit capability to support the Russian Phobos missions. The C-band uplink was

Table 5-7. Additional antenna losses.

Source	Loss (dB)
Surface rms (97 percent)	0.13
Spar and subreflector blockage (88 percent)	0.56
Feed dissipation losses (98 percent)	0.09
Feed-mode losses (96 percent)	0.18
Total additional loss	0.96

designed to handle a maximum power of 15 kW, while the L-band channel is receive-only. The C-band feed consists of a disc-on-rod antenna, which is located in the center of the existing L-band horn. The design of the feed is given in [33] and the performance measurements in [34]. After Phobos mission support, the C-band transmitter was removed from the antenna and the original L-band-only feed restored. The L-band receive-only system is currently in use to support radio science.

5.7 The Upgrade from 64 Meters to 70 Meters

The Voyager spacecraft flyby of Neptune in 1989 required a substantial enhancement in DSN performance, and a portion of that performance enhancement was accomplished by the 70-m upgrade project. The project goal was to improve performance by 1.9 dB at X-band (8.4 GHz). This improvement was to be obtained by increasing the antenna diameter to 70 m, increasing the RF efficiency through shaping of the reflective surfaces, improving the main reflector surface accuracy through the use of high-precision panels, and redesigning the subreflector support structure (quadripod) to reduce shadowing on the main reflector.

The increase in diameter involved reinforcement of the elevation wheel and the inner 34-m-diameter reflector backup structure, replacement of the reflector outer radial ribs beyond this inner 34-m segment, and replacement of all the surface panels.

The new surface panels were fabricated and installed to within a 0.65-mm rms deviation from the theoretically desired shape. These panels were fabricated using an adhesive bonding technique that achieved individual panel surface tolerance of better than 0.12 mm. In addition to high performance at X-band, these precision panels will support effective operation at Ka-band (32 GHz)—the next higher frequency band allocated for future deep-space communications.

The new subreflector measured 8 m in diameter and weighed approximately 6000 kg. It was machined as a single piece of aluminum to within a surface tolerance of 0.15 mm.

The mechanical installation and erection work at all three antennas was followed by a period of measurement and adjustments of the surface panels to reduce the overall dish-surface alignment tolerance to a 0.5-mm goal. The initial surface setting resulted from installing the panels on adjustable standoffs, using optical theodolite measurements. In accordance with the project plan, this provided an effective performance slightly in excess of that of the original 64-m antenna. Then, a series of microwave holography measurements were obtained in conjunction with Eikontech Ltd., which “mapped” the antenna sur-

face, precisely determining deviations from theoretical. The deviation calculations were subsequently used to adjust the panel positions [35].

5.7.1 Design and Performance Predictions

The basic elements of the 64- to 70-m upgrade are shown in Fig. 5-22. The upgrade consisted of both mechanical and RF improvements aimed at providing a 1.9-dB gain improvement at X-band and a 1.4-dB gain improvement at S-band, while suffering no adverse effects due to wind and gravity deformations [36]. A discussion of each element of the upgrade follows.

5.7.1.1 The 70-Meter Extension. The 64-m main reflector radial ribs were removed, beginning at a radius of approximately 15 m, and replaced with entirely new ribs to a final radius of 35 m. This nearly total replacement was driven by preassembly and field erection requirements to minimize time out of service. The physical area increase of the resulting instrument provides a +0.8-dB frequency-independent performance increase.

5.7.1.2 Structural Stiffenings. The original 64-m structural design, accomplished in the very early 1960s, was modeled on a computer and optimized based on a quarter-section analysis. This necessary limitation reflects machine capacity capabilities of that time. For the design of the upgrade, it was possible to model a half-section. Because of the twin elevation wheels necessary in a design employing a separately founded master equatorial pointing reference and control platform (rising to the intersection of azimuth and elevation axes), the symmetric half-section computer model was superior to the quarter model. Accordingly, some structural bracketing within the inner 15-m radius zone (so-called box girder) was identified as beneficial in further limiting gravitational

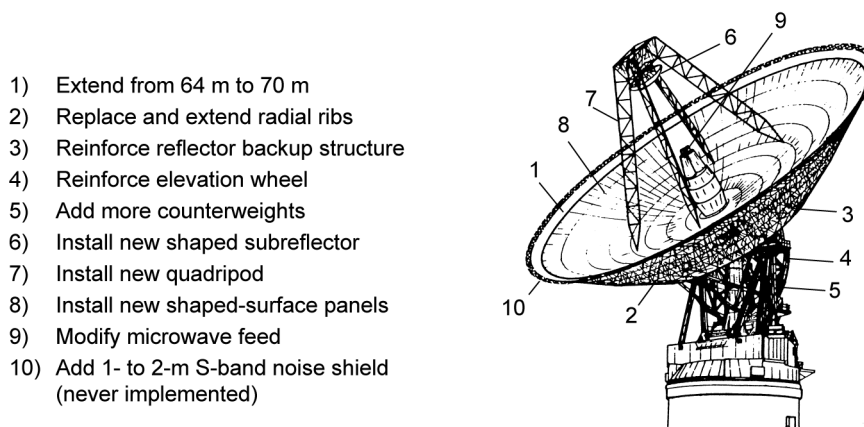


Fig. 5-22. 64-m to 70-m antenna extension.

distortions as a function of elevation angle. At X-band and at 10- and 80-deg elevation angles, the improvement was approximately +0.3 dB.

5.7.1.3 Improved Reflecting Panels. The existing 64-m reflecting panels were measured to be approximately 0.9-mm rms, leading to an X-band loss factor of nearly 0.5 dB. Considerably better manufacturing and installation accuracies were possible, with 0.25 mm or better achievable for the manufacturing portion. Although conventional civil engineering (theodolite) techniques were used initially to provide an X-band-quality surface, a microwave holographic technique was later applied, using strong available sources in geosynchronous Earth orbit, to fine-tune reflecting-panel settings. The combination of improved panel manufacturing and setting accuracies increased X-band gain by +0.5 dB.

5.7.1.4 Automated Two-Axis Focusing. For many years, DSN 64-m X-band operations were conducted by first manually activating the axial (z) focus, as elevation angle was changed, and later by automating this function. Conceptually, this maintained the subreflector rear focus in necessary juxtaposition with the more limber and moving main reflector focus, as a function of elevation angle. A careful structural analysis, involving main reflector best-fit paraboloid focus together with quadripod feed support and subreflector unit deflections, identified the value of lateral (y-axis or gravity-vector) focusing as well as axial focusing. However, lateral focusing produced a beam shift of the final ensemble radiation pattern, necessitating a pointing feedback correction. A new microprocessor-based table lookup/compare/feedback machine was developed for this purpose. The performance benefits at X-band were similar in nature and magnitude and additive to those achieved by the structural stiffening activity mentioned above.

5.7.1.5 Improved Quadripod Feed Support. In order to accommodate a different (shaped) subreflector, significant changes were necessary in the apex region of the existing quadripod structure. Again, based on the important constraint for short out-of-service time, it became optimal to have a completed all-new structure that could be rapidly installed. Further, having the system on the ground enabled preassembly and test of the automated two-axis focusing subsystem. Because of the upgrade, advantage was taken to provide a reduced shadow (blocking) design. An anticipated improvement of 0.3 dB was calculated for this change.

5.7.1.6 Optional Main Reflector Noise Shield. In the initial design trade-offs, a noise shield to improve S-band performance was considered but deleted due to economic considerations.

5.7.1.7 Shaped Dual-Reflector Design. Techniques have been available since the mid-1960s to synthesize by geometrical optics (GO) uniform aperture illumination of a two-reflector antenna. However, the 70-m antenna presented a difficult shaping problem because of the asymmetric geometry and the RF design constraints required by economic considerations.

To minimize feed costs, it was necessary to leave the basic feed geometry unchanged; that is, both the cone tilt angle and the height of the feed had to remain the same. The solution had to best-fit to the existing 64-m contour so the basic inner structure would remain the same. The main reflector was to be symmetrical and 70 m in diameter. The basic design trade-offs considered the subreflector size, a subreflector flange versus a noise shield, and an asymmetric versus a symmetric subreflector [37]. Furthermore, since shaping uses GO, which is independent of frequency, it was necessary that all the feeds have the same radiation pattern. All the feeds on the antenna matched the standard 22-dB horn pattern, except the X-band feed, which had been converted to a dual multimode horn design to obtain 0.36 dB over the standard design. However, since the shaping converted any radiation pattern into uniform illumination, it was decided to convert the X-band feed horn back to a standard 22-dB horn pattern and base the shaping upon the standard pattern.

The first step of the basic synthesis technique was to determine the main reflector shape using main and subreflector symmetric synthesis. This design then was optimized for X-band gain and noise temperature [38]. An important parameter was the subreflector illumination angle, which determined the subreflector size. Table 5-8 delineates the subreflector size trade-off. An illumination angle of

Table 5-8. Theoretical 22-dB feed-horn pattern used to shape and scatter.
Option selection is shaded in gray.

Parameter		Options Studied				
Subreflector illumination angle (deg)	15	16	17	18	19	
Subreflector diameter (m)	7.1	7.68	8.26	8.84	9.45	
S-band (2.295 GHz)						
Efficiency (percent)	Not calculated	90.2	90.4	91.4	90.4	
Noise temperature (K)	Not calculated	3.6	3.6	4.5	5.3	
X-band (8.45 GHz)						
Efficiency (percent)	91.1	92.4	92.5	90.6	85.9	
Noise temperature (K)	Not calculated	0.67	0.52	0.6	1.8	

16 deg was chosen (versus 17 deg for the 34-m antenna design) to minimize the subreflector size while achieving nearly optimum performance. Second, a new subreflector design was computed by putting the feed point in the offset position and synthesizing an asymmetric subreflector by ray tracing for perfect phase [39], using the previously determined main reflector. The basic geometry of the synthesis is shown in Fig. 5-23. Since only phase synthesis was used, the amplitude illumination was slightly tilted, but the loss due to the tilt was negligible [40].

To minimize the cost of the implementation, the X-band dual-hybrid-mode horn was not directly replaced with a standard 22-dB feed horn because the phase center location of the standard feed horn would require moving the input flange and associated equipment. Rather, a standard-design feed horn was mated with an input flange and the phase center moved to the proper location through the use of a feed-horn extension termed a stovepipe design [41]. There was a slight degradation in gain, but the loss was deemed acceptable to reduce the cost. As shown in Table 5-9, detailed design expectations were 75.8 percent aperture efficiency at S-band and 71.1 percent at X-band.

5.7.2 S- and X-Band Performance

The measured S-band efficiency was 75.6 percent \pm 0.8 percent. Compared with previous performance, a 1.91-dB improvement was obtained at S-band. For X-band, the three antennas had an efficiency of 68.7 percent \pm 1.5 percent [42]. Compared with previous 64-m performance, an average improvement of 2.13 dB at X-band was obtained. Figure 5-24 shows the measured X-band 70-m gain performance for the three antennas, together with the nominal design expectation.

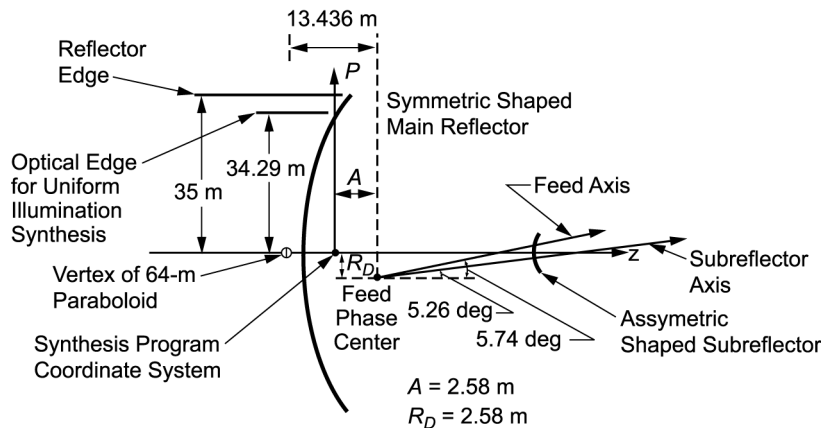
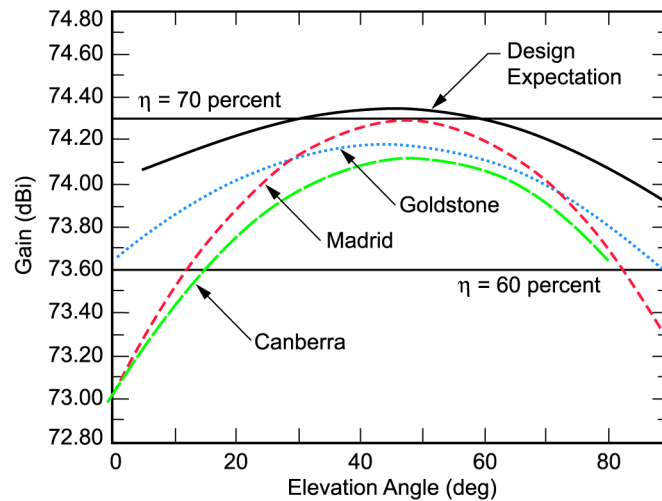


Fig. 5-23. 70-m antenna geometry used in physical optics analysis.

Table 5-9. Design-expected S-/X-band 70-m efficiency performance.

Gain Factors	S-Band	X-Band	Notes
Rear spillover	0.994	0.997	None
Forward spillover	0.959	0.964	None
Illumination amplitude	0.959	0.982	Standard feed horn
Illumination phase	0.994	0.989	None
Cross-polarization	1.00	1.00	None
$m \neq 1$ modes	0.980	0.996	None
Central blockage	0.983	0.988	None
Quadripod blockage	0.9008	0.9008	5.1 percent effective
Dichroic reflectivity	0.9993	N/A ^a	Below plane reflector
Surface reflectivities	0.998	0.998	None
Surface tolerances	0.9946	0.9527	None
Pointing squint	0.996	1.000	X-band beam peaked
Waveguide dissipation	0.9795	0.984	None
Waveguide VSWR	0.9908	0.9908	None
Dichroic VSWR	N/A	0.990	None
Compromise feed horn	N/A	0.975	Stovepipe extension
Total	0.758 (+63.28 dBi at 2.295 GHz)	0.711 (+74.34 dBi at 8.42 GHz)	None

^aNot applicable.**Fig. 5-24. X-band measured gain performance for DSN 70-m antennas.**

In addition to the large improvement in aperture efficiency, somewhat lower total system operating noise levels were obtained: approximately 1.5- and 0.7-K improvements at S- and X-bands, respectively. The best measurements at S-band show a 18.3-K total at zenith and about a 21-K total at 30-deg elevation. At X-band, all three antennas are quite uniform at $20.9 \text{ K} \pm 0.3 \text{ K}$ at zenith and about 25.5 K at 30-deg elevation. Figure 5-25 shows system-noise levels with elevation angle. The two upper curves are total operating system-noise levels (with atmosphere) while the lower curves have the nominally clear-dry atmosphere numerically removed. The lower curves are indicative of acceptably small antenna spillover and scattering-noise components.

A very important element of this project was the application of the microwave holographic technique. Holographic imaging was achieved by use of 12-GHz-band geostationary satellite beacon signals providing approximately 75-dB signal-to-noise ratio (SNR) on beam peak, with over 40-dB SNR in the reference channel. Imaging was used for adjustment of the nearly 1300 individual reflector panels on each antenna. Additionally, holographic imaging provided data for quantifying the aperture illumination uniformity, the blockage and diffraction phenomena, the rotating subreflector alignment quality, gravity loading, and excellent estimates of the achieved surface tolerance following adjustment. At high lateral resolution (0.42 m), the surface tolerance achievable, presuming infinite ability to adjust, is found to be 0.3-mm rms. This is essentially the panel manufacturing precision together with a holography data system noise component. It was believed that the achievable surface tolerance was about 0.4-mm rms for these antennas. However, due to time constraints,

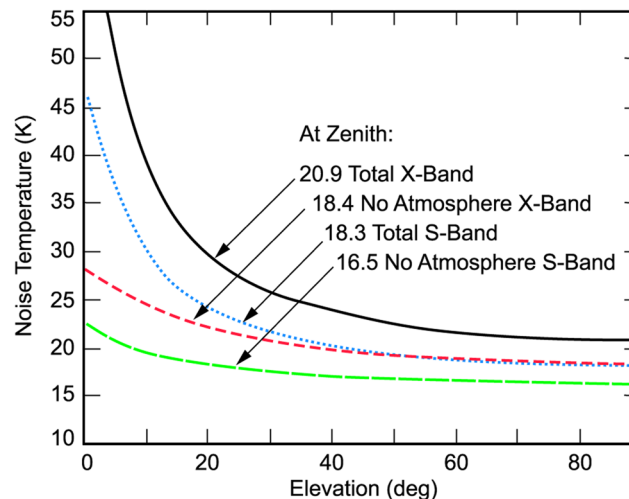


Fig. 5-25. 70-m antenna system-noise level.

the goal was to meet only the project specification, which was 0.65-mm rms at 0.42-m resolution. Effectively, surface adjustments were not refined for the last available 0.1 dB at X-band. A photograph of the 70-m antenna at Goldstone is shown in Fig. 5-26.

5.7.3 Ka-Band Performance

In 1989, a 32-GHz receiver was installed on the 70-m antenna at Goldstone. The primary purpose of the installation was to measure the high-frequency performance of the antenna after it was upgraded and enlarged from 64 m to 70 m. System calibrations were performed, and several radio sources were measured between March and July of 1989. The measurements were highly repeatable, which suggests that the precision of the data is about 2.5 percent. The peak of aperture efficiency function at 32 GHz is 0.35 ± 0.05 centered around a 45-deg elevation (Fig. 5-27). The estimated error (2 sigma) of the efficiency number was dominated by the uncertainty in the absolute flux-density calibration. Further details can be found in [43].

5.7.4 Adding X-Band Uplink

Prior to 1999, the X-band system on the 70-m antenna was receive-only. X-band uplink (7.145–7.190 GHz) had been available on DSN 34-m antennas since the mid-1980s (starting with the 34-m high-efficiency antenna described in Chapter 6 of this monograph). However, in 1995, due to the advent of

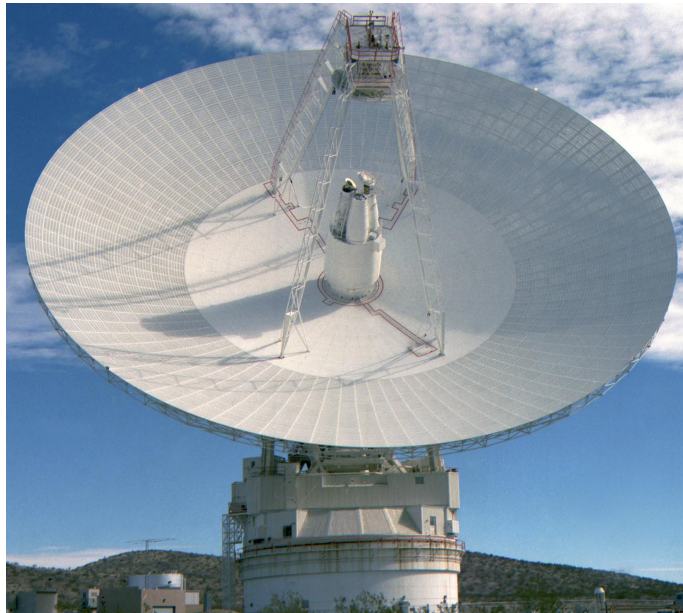


Fig. 5-26. The 70-m antenna after the 64- to 70-m upgrade.

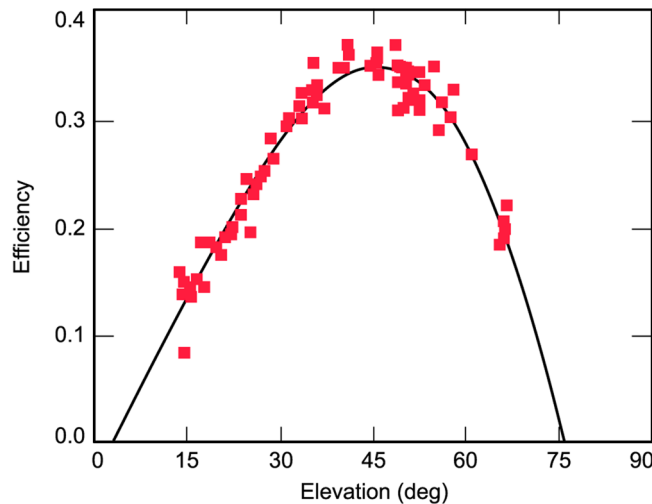


Fig. 5-27. The 70-m antenna's 32-GHz efficiency as a function of elevation angle.

smaller spacecraft requiring higher data rates and the need for high-power X-band for emergency situations, the National Aeronautics and Space Administration (NASA) funded JPL to implement a 20-kW X-band uplink on all 70-m antennas. There were two difficulties with X-band uplink on the 70-m antenna: (a) the existing dichroic plate could only pass the downlink frequency, so a new dichroic plate design was required that could pass both the uplink and downlink frequencies, and (b) the additional noise temperature from a traditional diplexer implementation might be as large as 9 K. To circumvent the additional noise temperature caused by a traditional diplexer, a new ultralow-noise-diplexed X-band microwave system [44], called the X-/X-band (X/X) diplexing feed was developed for the 70-m antenna uplink.

5.7.4.1 New Deep Space Network X/X Diplexing Microwave Feed. An excellent discussion of the benefits of the new feed versus a traditional DSN diplexer can be found in [44]. The significant advantage comes from the ability to cryogenically cool most of the components in the downlink signal path.

Figure 5-28 shows a simplified block diagram of the X/X diplexing microwave feed. A diplexing junction is used for combining the uplink and downlink signals. This diplexing junction is a six-port device. Two of the ports use circular waveguides. One is connected to a 22-dB feed horn through a coupler, and the other is connected to the LNA package through a transmitter reject filter and an ambient-load sliding switch. The filter provides 40 dB of rejection for the fundamental transmitter frequency. The ambient-load switch is used for calibration of the LNAs. The other four ports, which are in rectangular

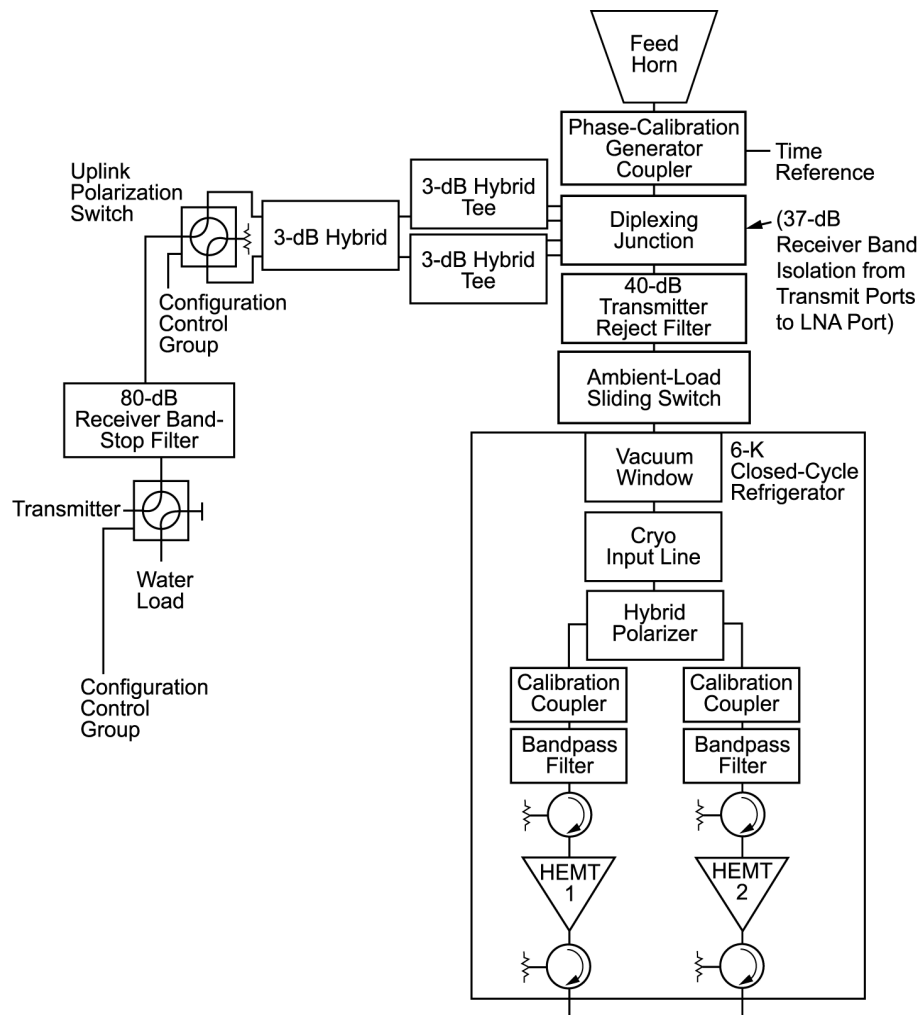


Fig. 5-28. Simplified block diagram of the X/X diplexing feed.

waveguides, are used for injection of the uplink signal. These ports are combined into one port with a network of hybrids, tees, and a polarization selection switch. For additional protection against the spurious signal generated by the transmitter, an 80-dB absorptive filter is used between the polarization switch and the transmitter.

In the downlink path, the signal coming out of the ambient load switch is guided to the LNA package. The LNA package consists of a cryogenically cooled container that holds the rest of the downlink path components. These components include a polarizer and orthomode junction to convert the circularly polarized signal to linear polarization, additional bandpass filters for pro-

tection of the super-sensitive high-mobility-electron transistor (HEMT) LNAs, and circulators for improving the match and reducing the standing wave generated between the reflective filters in the downlink path. One LNA is used for the RCP signal, the other for the LCP signal.

The noise contribution of the microwave circuit in this feed is approximately 2.7 K for diplexed operations. Table 5-10 shows the breakdown of the predicted and measured noise temperature of the individual components of this feed at 8.45 GHz.

Table 5-10. Noise-temperature breakdown of X/X diplexing feed components, in kelvins.

Item	Predicted Noise Temperature	Measured Noise Temperature
Feed horn	1.0	0.8
Phase-calibration-generator coupler	0.3	0.3
Diplexing junction and filter	1.7	1.4
Ambient load switch	0.2	0.2
LNA	6.0	8.4
Total	9.20	11.1

5.7.4.2 S-/X-Band Dichroic Mirror. Prior to 1999, the 70-m antennas supported downlink only. Therefore the dichroic mirror utilized in the reflex–dichroic feed system was a narrowband design capable of reflecting both the S-band transmit and receive frequencies while only passing the X-band downlink band. With the new diplexed microwave feed, the antenna needed a wideband dichroic plate that would pass the X-band uplink frequencies (7.145–7.190 GHz) as well as the downlink frequencies, with very little loss.

A new dichroic plate that uses cross-shaped holes to provide low loss and minimizes grating lobes for both the uplink and downlink bands was designed [45]. Figure 5-29 shows the perforated section of this dichroic plate. It was fabricated in hard, oxygen-free copper, using a wire electric discharge machine.

Cross-shaped holes can be packed tighter than circular holes and, therefore, it is possible to design a wideband dichroic plate that can support X-band uplink and downlink bands without undesired grating lobes. Figure 5-30 shows the theoretical and measured power reflection coefficient of this mirror for a circularly polarized signal incident at a 30-deg angle with respect to the normal to the plane of the mirror [45]. As can be seen, the mirror is designed to have two resonant frequencies: one at the center of the uplink band, the other at the center of the downlink band. There is excellent agreement between the theoret-

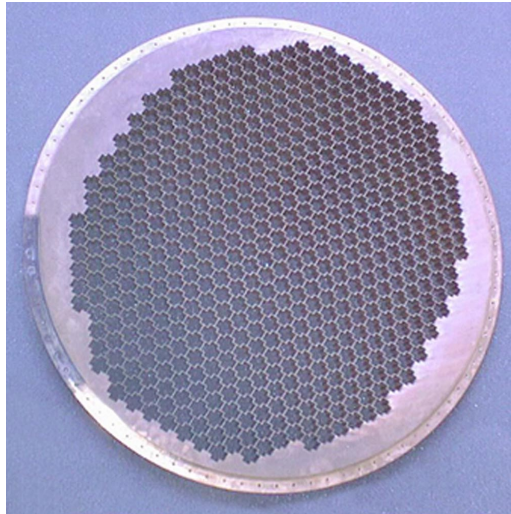


Fig. 5-29. The wideband S-/X-band dichroic mirror.

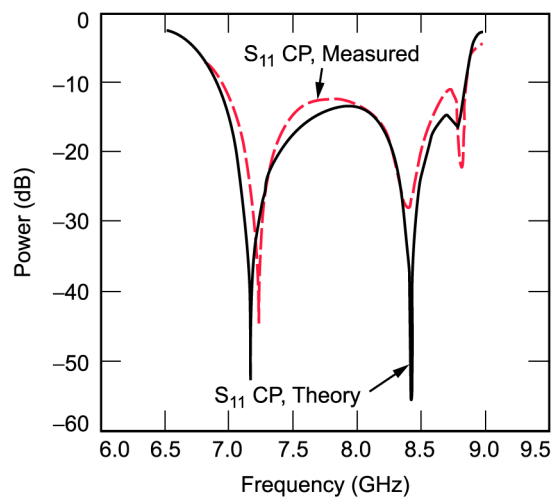


Fig. 5-30. Power reflection coefficient: comparison of measurement and theory for circular polarization (CP).

ical and measured values. The error between the theoretical and measured resonant frequencies is less than 1 percent. However, when the feed cone containing the dichroic plate was tested on the ground prior to installation on the antenna, there was a significantly higher noise temperature than initially

anticipated. This higher noise temperature was later confirmed by measurements on the dichroic plate alone [46].

The noise-temperature contribution of the dichroic plate is the result of two effects: (a) ohmic loss as the signal propagates through the holes in the plates and (b) the mismatch or scattering loss of energy that is reflected from the plate surface. The ohmic loss tends to be small, contributing less than 1 K.

The scattering loss from the rear surface of the plate is quite large and would contribute 12 to 18 K of noise if the scattered energy were to see ambient temperature. Fortunately, when located on the 70-m antenna, the rear scatter is largely reflected to the sky and causes a small (1-K) contribution. The noise-temperature contribution can be used to estimate the antenna efficiency loss due to the plate. A 12 to 18 K contribution corresponds to an efficiency loss of 4 to 6 percent (0.2 dB). This is consistent with the measurements of the antenna efficiency with and without the plate in place.

Since the dichroic plate is only required for simultaneous S- and X-band operation, the plate was made retractable, as shown in Fig. 5-31, to provide for high-performance X-band-only operation.

5.7.4.3 Radio Frequency Performance. A 20-kW X-band uplink capability was installed on all three 70-m antennas: at Goldstone and Canberra in 2000 and at Madrid in 2001. The intent was to have minimal impact at all other frequencies, and this was accomplished utilizing the new retractable dichroic plate and X-/X-band feed. The critical X-band receive performance is summarized in Table 5-11 for noise temperature and Table 5-12 for gain. All three antennas are capable of transmitting 20 kW on the uplink.

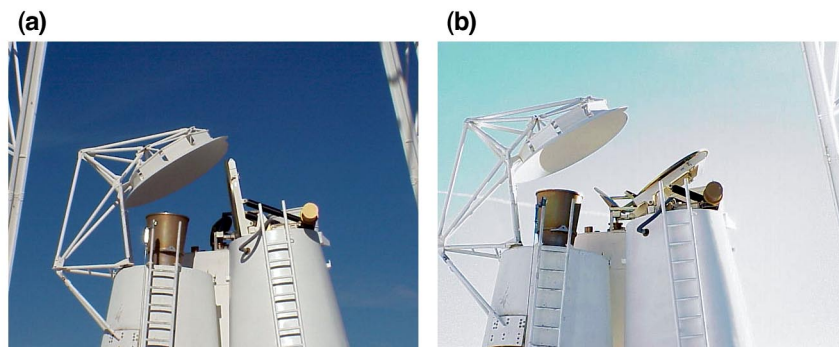


Fig. 5-31. The dichroic plate retraction mechanism:
(a) retracted and (b) extended.

Table 5-11. X-band downlink performance post-installation: noise temperature, in kelvins.^a

Operation Mode (T_{op} [SNT ^b , in vac, at zenith, K])	DSS-14				DSS-43				DSS-63					
	Predicted	Measured at LNA Input		Measured at Horn Aperture	Measured at LNA Input	Measured at Horn Aperture	Measured at LNA Input	Measured at Horn Aperture	Measured at LNA Input	Measured at Horn Aperture				
		LNA-1	LNA-2	LNA-1	LNA-2	LNA-1	LNA-2	LNA-1	LNA-2	LNA-1	LNA-2			
X-band-only mode, transmitter off	14.2	14.22	14.22	14.35	14.35	14.35	14.57	14.57	14.7	14.7	13.76	14.05	13.89	14.18
S-/X-band mode, transmitter off	15.4	15.12	15.12	15.26	15.26	15.26	15.77	15.78	15.92	15.93	15.03	15.11	15.18	15.26
Noise temperature increase, transmitter on	<0.1	<0.2	<0.2	N/A ^c	N/A	N/A	<0.2	<0.2	N/A	N/A	<0.2	<0.2	N/A	N/A

^aCourtesy of Manuel Franco.
^bSNT = system noise temperature, vac = vacuum.
^cNot available.

Table 5-12. X-band downlink performance at LNA-1 post-installation: gain, in dBi.^a

		DSS-14				DSS-43				DSS-63			
Elevation Angle (deg)	Predicted	Measured at LNA Input		Measured at Horn Aperture		Measured at LNA Input		Measured at Horn Aperture		Measured at LNA Input		Measured at Horn Aperture	
		Dichroic Plate	Dichroic Plate	Dichroic Plate	Dichroic Plate	Dichroic Plate	Dichroic Plate	Dichroic Plate	Dichroic Plate	Dichroic Plate	Dichroic Plate	Dichroic Plate	Dichroic Plate
		Retracted	Extended	Retracted	Extended	Retracted	Extended	Retracted	Extended	Retracted	Extended	Retracted	Extended
10	74.0	74.04	73.84	74.08	73.88	74.25	73.98	74.29	74.02	74.01	73.57	74.05	73.61
25	74.2	74.22	74.02	74.26	74.06	74.47	74.20	74.51	74.24	74.46	73.98	74.50	74.02
45	74.2	74.30	74.10	74.34	74.14	74.55	74.28	74.59	74.32	74.67	74.19	74.71	74.23
80	73.9	74.04	73.84	74.08	73.88	74.11	73.84	74.15	73.88	73.96	73.61	74.00	73.65

^aCourtesy of Manuel Franco.

5.8 Distortion Compensation

As is well illustrated in Fig. 5-27, a problem with Ka-band is the significant loss in efficiency at low and high elevation angles due to the gravity-induced deformations of the primary antenna surface.

There are a number of techniques that can be employed to compensate for large-scale surface errors in large reflector antennas. One approach to gravity compensation is to install actuators at the corners of each main reflector panel or at the panel junctions. The actuators can either be controlled open loop if there is a prior knowledge of the surface errors or in a closed-loop system if the surface is actively measured. This approach has been implemented on the clear-aperture 100-m antenna at Greenbank, West Virginia [47].

A second approach for gravity compensation is to install a deformable sub-reflector. This approach has been implemented at MIT's Haystack antenna and is one of the proposed solutions for the 25-m ARISE (Advanced Interferometry between Space and Earth) antenna operating at 86 GHz [48].

Since the early 1990s, extensive work [49–53] has been performed at JPL on the use of a deformable mirror to correct for the gravity-induced distortions on a large reflector antenna. This work culminated in a demonstration of a deformable mirror on the NASA/JPL 70-m antenna in early 1999 [54,55]. The deformable mirror, nominally a flat plate, is placed in the beam path and deformed in order to compensate for the gravity-induced distortions as the antenna moves in elevation. Actuators on the mirror are driven via a lookup table. Values in the lookup table are derived using the distortions, ray tracing, and a structural finite element model of the mirror system.

During the same period, an array-feed compensation system (AFCS) was also studied extensively at JPL as an alternative to the deformable mirror approach for gravity compensation [56–58]. The system consists of a small array of feed horns, LNAs, downconverters, and digital-signal-processing hardware and software for optimally combining the signals received by the feed horns.

A combined system consisting of a deformable flat plate (see below) and the AFCS was also demonstrated on the 70-m antenna. The combined system worked better than either one of the systems acting alone [59,60].

A comprehensive study was undertaken [61,62] that considered each of the possible options for implementing Ka-band on the existing 70-m antennas. The study described the advantages and disadvantages of each approach and estimated the relative cost and RF performance.

5.8.1 Deformable Flat Plate

The deformable flat plate (DFP) is a deformable mirror designed to correct gravity-induced antenna distortions on the main reflector surface by correcting wavefront phase errors. An experimental DFP (Fig. 5-32) was built with actua-

tors laid out to enable gravity correction for either the 70-m or the DSS-13 34-m DSN antennas [51]. The DFP surface was constructed from a 6000-series aluminum sheet, 0.04-in. (1-mm) thick and 27 in. (68.6 cm) in diameter, nominally producing a flat surface. The plate is driven by 16 actuators, via a lookup table, that change as a function of antenna elevation angles. Open-loop calibration of the DFP is achieved by following these steps:

- 1) Model the RF distortions of the main reflector (base this model upon measured holography maps of the 70-m antenna obtained at three elevation angles); process the holography maps, using an appropriate mechanical model of the gravity distortions of the main reflector to provide surface-distortion maps at all elevation angles (this technique is further described in [63])
- 2) From the surface-distortion maps, use ray optics to determine the theoretical shape of the DFP that will exactly phase-compensate the distortions
- 3) Using the theoretical shape and a NASTRAN mechanical model of the plate, select the actuator positions that generate a surface that provides the best rms fit to the theoretical model (using the actuator positions and the NASTRAN model provides an accurate description of the actual mirror shape, permitting the performance of the DFP to be determined [55]).

5.8.2 Array-Feed Compensation System

The AFCS comprises a feed array and cryogenic dewar, downconverter assembly, and digital-signal-processing assembly (DSPA). The feed array con-

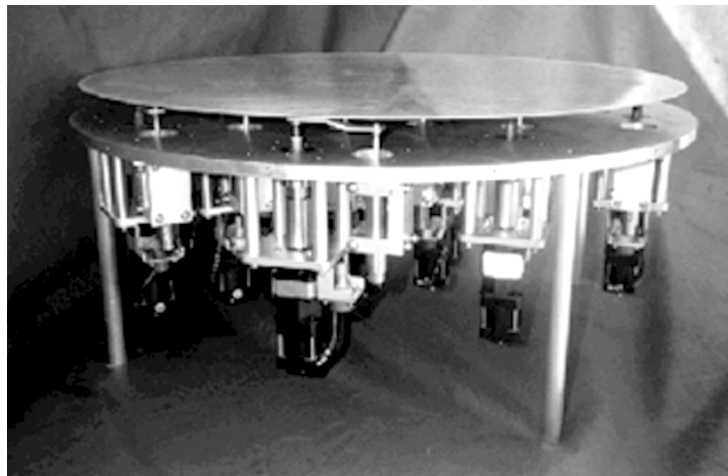


Fig. 5-32. Experimental DFP.

sists of seven identical, smooth-walled Potter horns, each 1.732 in. (4.4 cm) in diameter, providing 22-dBi gain at 32 GHz. The wall of each feed horn is tapered near the top to facilitate close packing, minimizing the loss of signal energy between horns. The cryogenic front end contains three-stage HEMT LNAs that provide 25 dBi of total gain, thus establishing high SNR without adding significant receiver noise to the signal. Each HEMT LNA outputs an amplified RF signal at 32-GHz center frequency, which is then translated to 300-MHz intermediate frequency (IF) by the seven-channel downconverter assembly and transmitted to the DSPA. The DSPA estimates the combining weights in real time and combines the weighted digital samples to produce a “combined output” with improved SNR. A photograph of the feed array prior to installation in the cryogenic dewar is shown in Fig. 5-33.

5.8.3 The Array-Feed Compensation System–Deformable Flat-Plate Experiment

During the period from November 1998 through February 1999, a series of measurements was made on the 70-m antenna at DSS-14 to determine the performance characteristics of two systems designed to compensate for the effects on antenna gain of elevation-dependent gravity distortion of the main reflector. The AFCS and DFP were mounted in the same feed cone, and each was used

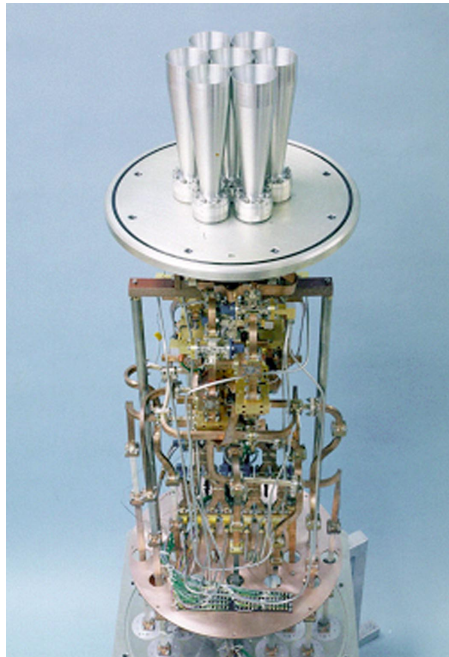


Fig. 5-33. Feed array for the AFCS.

independently as well as jointly to measure and improve the antenna aperture efficiency as a function of elevation angle. The experimental data is presented in [54,58] and the theoretical formulation in [55].

The experiment geometry is shown in Fig. 5-34. The main elements are the 70-m main reflector and subreflector, a refocusing ellipse, the DFP, and the receive feed system. The focal point of the dual-reflector 70-m system is labeled F_1 , and the focal point where the feed is placed is labeled F_2 . The antenna Cassegrain focus was 0.6 in. (1.5 cm) above F_1 , which was corrected by z-axis alignment of the subreflector. Looking at the system in the transmit mode, the output of the feed system is refocused at F_1 , the input to the dual-reflector system. The parameters of the ellipse are chosen to map the fields (with no magnification) from F_2 to F_1 . Hence, the performance of the 70-m system would be the same if the same feed were placed at either F_1 or F_2 . Experiments were done with the AFCS placed at both F_1 and F_2 . When the AFCS was placed at F_2 , combined AFCS–DFP performance measurements were possible.

5.8.3.1 AFCS Antenna Deformation Compensation. The New Millennium Program spacecraft, Deep Space 1 (DS1), provided a stable Ka-band signal throughout the holography cone experiments. During a typical DS1 track, it

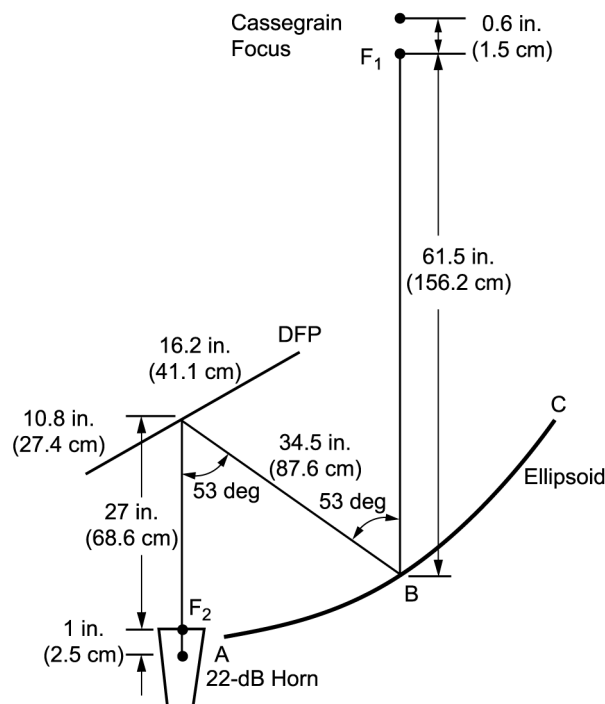


Fig. 5-34. Experimental geometry for the 70-m experiment.

was necessary to update antenna pointing in real time, using the coherent version of the array-feed boresighting algorithm [58]. In addition to providing pointing information, this algorithm records the complex signal voltages at the end of each integration time in all seven channels as well as in the combined channel, measures rms noise voltages, and updates optimum combining weights. This data can be used to compute the combining gain, G_c , which is defined as the ratio of the SNR of the combined channel to the SNR of the central channel, and is an important quantity for characterizing AFCS performance.

A representation of combining gain data recorded during the DS1 holography cone experiment is shown in Fig. 5-35. Note that above 60-deg elevation, the data appears to split into two branches, indicating an azimuth dependence in the combining gain: the upper branch corresponds to the ascending part of the track (before transit), and the lower branch corresponds to its descent towards the horizon (after transit). This asymmetrical behavior of the antenna has been observed on all occasions, but the exact cause is not well understood at this time. The third-order trend line indicates average gain at a given elevation, without taking into account the azimuth dependence of the gain curve at higher elevations. Also shown on the curve is the predicted combining gain, using the holography-determined distortions and the computed feed-horn pattern.

5.8.3.2 DFP Compensation. As indicated above, the computation of the required deformable-mirror surface begins with a map of the main-reflector distortions to be corrected for at the elevation angle of interest. The final output

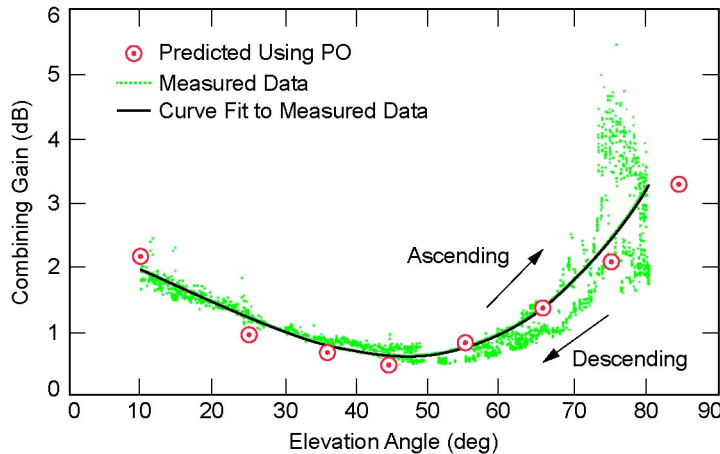


Fig. 5-35. Computed and measured performance of the AFCS on the 70-m DSS-14 antenna at 32 GHz.

of the design process is the actuator settings required to correct for these distortions.

The gravity deformations of the antenna at all elevation angles are derived from holography measurements taken at only three elevations: 47.2, 36.7, and 12.7 deg [63]. The computations assume that

- The antenna structural response due to gravity loading is linear
- The antenna response to gravity loading is symmetric relative to the antenna elevation-rigging angle
- The elevation-rigging angle (maximum gain) of the antenna can be accurately inferred from total power radiometry (TPR) efficiency measurements.

Note that in the absence of measurement noise, three is the minimum number of angle observations needed to solve for the three unknowns in the linear model used.

In the usual case where noise is present, it is desirable to acquire measurements at more than three elevation angles so that a least-squares solution can be obtained. Conversely, if only three measurements can be made, making two of them near the extreme values of 0 and 90 deg will produce the most accurate results. Due to the constraints of time and the highest viewable angle (47 deg) available from this antenna location, neither of these conditions could be met at the time of the holography cone experiment at DSS-14; therefore, the second and third conditions listed above were added to the derivation.

A typical holography distortion map is shown in Fig. 5-36(a). There is a significant random component in the surface that cannot be compensated for with a smoothly varying DFP surface. Consequently, a 91-term Zernike polynomial description of the main reflector antenna was used to design the DFP. The Zernike representation for the main reflector surfaces is shown in Fig. 5-36(b) for the 15-deg elevation. The difference from the full holography map representation of the dish and the Zernike representation is shown in Fig. 5-36(c). This component of distortion will not be corrected by the DFP.

The values in the actuator lookup table were computed by performing a ray trace from the deformed main reflector, represented by Zernike polynomials, to the DFP position and using the structural finite element model of the mirror [55]. This process was repeated at 5-deg-elevation increments to derive 17 sets of 16 actuator displacements. The performance of the DFP was assessed by tracking natural radio sources and obtaining antenna temperature using TPR [54]. Positive compensation was achieved over all elevation angles, with average compensations at Ka-band of 1.7 and 2.3 dB, at elevation angles of 10 and 80 deg, respectively. These results successfully demonstrate an open-loop calibration of the DFP (Fig. 5-37).

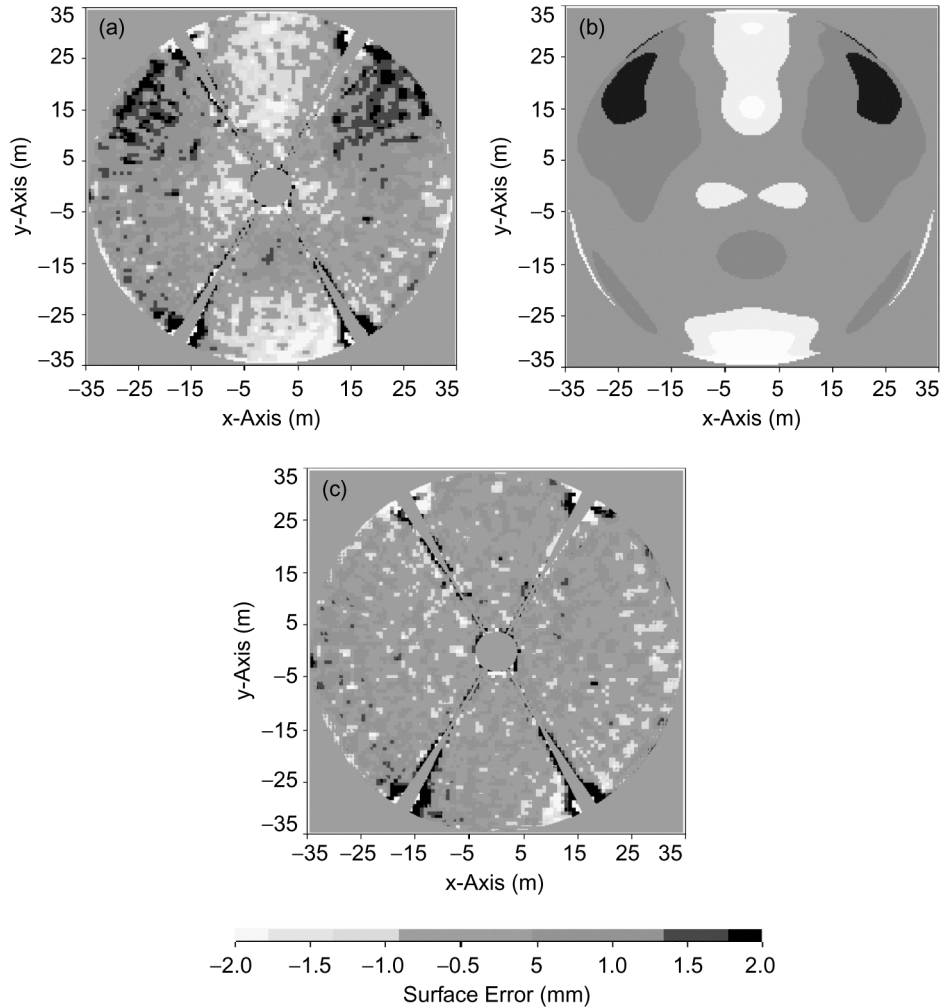


Fig. 5-36. Main reflector distortion at an elevation of 15 deg:
(a) full holography, (b) Zernike polynomial representation,
and (c) the difference between the two surfaces.

After completion of the AFCS–DFP experiment, another method (ranging theodolite) was used to measure the main-reflector distortion. This time, the measurements were made at widely scattered elevation angles (13, 30, 47, 68, and 88 deg), and thus it was not necessary to assume the second and third conditions listed above. These measurements also served as a verification of the assumptions. As might be expected, these holography-derived results at high elevation angles were less accurate than the results at angles below 47 deg. Although it was too late to use the theodolite data to recompute the DFP actua-

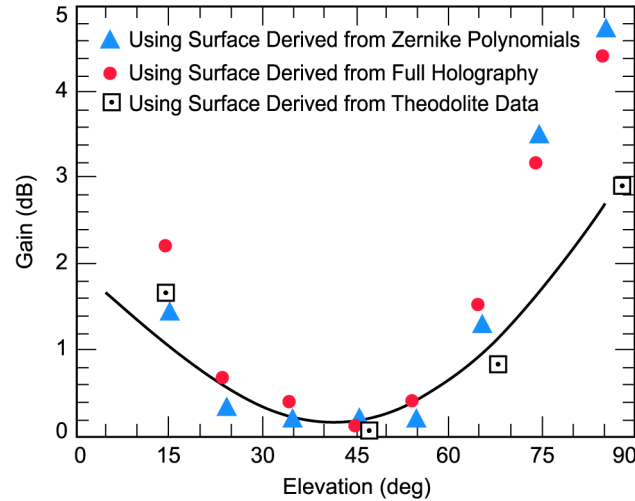


Fig. 5-37. Computed and measured performance of the DFP on the 70-m DSS-14 antenna at 32 GHz.

tor positions, a more accurate assessment of the expected performance was made using the more accurate characterization of the distortion at high elevation angles. Also shown in Fig. 5-37 is the predicted performance using the main-reflector surface derived from the theodolite measurements. As can be inferred from the data, if the more accurate main-reflector distortion was used to compute the actuator positions, better performance would have been achieved at higher elevation angles, using the DFP.

5.8.3.3 Joint AFCS–DFP Performance Measurements. As we have shown, operating either the AFCS or the DFP singly provides some gravity compensation over all elevation angles. However, the performance of a combined AFCS–DFP system was significantly better than each one performing individually. Analysis of the data obtained on day of year (DOY) 056 (Table 5-13), when DS1 was tracked continuously as it descended from an elevation of approximately 50 deg to 8.5 deg, clearly demonstrates that an AFCS–DFP compensation system working together in real time can recover most of the signal energy lost to gravitational deformations on the 70-m antenna at Ka-band. The various gains used in Table 5-13 are defined as follows:

$G_{AFCS} = G_c$ is the improvement over the central channel when the DFP is flat

G_{DFP} = the increase in signal power in the central channel when the DFP is activated

G_{joint} = the improvement over the uncorrected central channel when the DFP and the AFCS operate jointly to recover SNR losses

Table 5-13. Average combining gain of AFCS, DFP, and AFCS–DFP on DOY 056, in decibels.

Elevation (deg)	G_{AFCS}	G_{DFP}	G_{joint}	$\Delta AFCS$	ΔDFP
8.5	2.1	1.8	2.9	1.1	0.8
13	1.8	1.6	2.5	0.9	0.7
16.5	1.6	1.4	2.2	0.8	0.6
23	1.2	1.1	1.8	0.7	0.7
28	1.1	0.9	1.5	0.6	0.4
33	0.75	0.6	1.0	0.4	0.25
38	0.5	0.3	0.6	0.3	0.1

$\Delta AFCS$ = the contribution of the AFCS to G_{joint} over that of the DFP acting alone

ΔDFP = the contribution of the DFP to G_{joint} over that of the AFCS acting alone.

The computed versus measured results for the combined DFP–AFCS are shown in Fig. 5-38. There are several curves shown on the figure. The lower solid curve is the measured baseline efficiency. The calculated results for the combined DFP–AFCS, using the full holography maps are shown in circles. The measured performance of the combined DFP–AFCS system is shown, but only data for lower elevation angles was obtained. Observe that the measured and calculated values agree to within a few percent. It should be noted that the measured efficiency curve includes a substantial random component. This random-component loss is estimated to be on the order of 3.4 dB. This estimate was derived by looking at the difference between the gain calculated by using a Zernike polynomial representation of the surface (smooth component) compared to the gain calculated using the surface derived from holography (containing smooth and random components). Also observe that the combined system recovers almost all of the gain lost due to the systematic distortion but does not recover the random component of the surface distortion. It is anticipated that a majority of the random component will be recovered by resetting the main reflector.

Also shown in Fig. 5-38 is the expected performance if a so-called “perfect DFP” were used. A perfect DFP means that the required shape of the plate as determined by the Zernike polynomial expansion of the main-reflector surface is replicated exactly. With an improved DFP, it should be possible to get close to the required surface and produce performance close to this prediction. The perfect DFP does not recover the random component of the distortion, as this distortion is not even included in its determination.

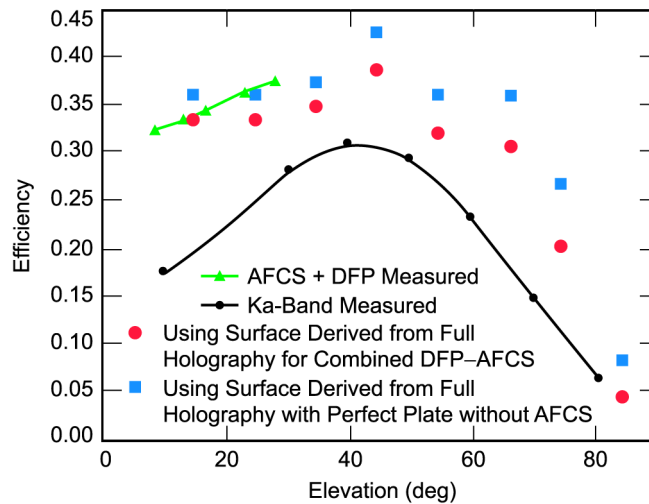


Fig. 5-38. Computed and measured performance of the combined AFCS–DFP system.

5.8.4 Projected Ka-Band Performance

The present aperture-efficiency performance of the DSS-14 antenna at Ka-band is marginal as a result of two independent effects: loss at the rigging angle due to the rms surface error of the main reflector and losses due to gravity-induced deformation (see Fig. 5-39, the lower curve, “Ka-Band Current”). The marginal rigging-angle aperture efficiency of 31 percent is mostly due to the main reflector rms error of 0.73 mm. It is expected that this rms error can be reduced to between 0.35 and 0.45 mm, thus increasing the overall antenna aperture efficiency to between 55 and 60 percent at the rigging angle (see Fig. 5-39, the upper curve, “Ka-band + PNL Set”). The curve labeled “AFCS + DFP Current” in Fig. 5-39 shows the gravity performance of the antenna with joint AFCS–DFP compensation obtained from Table 5-12, while the curve “AFCS + DFP + PNL Set” shows the expected efficiency performance when compensation is applied to the antenna after panel setting. Thus, with appropriate panel setting and gravity compensation benefits from both systems, the DSS-14 antenna can achieve excellent performance at Ka-band, thereby enabling the predicted 6-dB communications improvement relative to X-band.

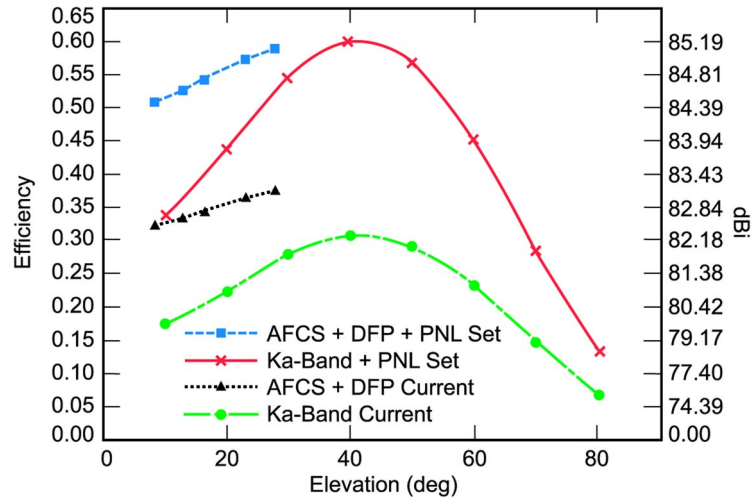


Fig. 5-39. Performance of the 70-m DSS-14 antenna, 32 GHz, present and future (predicted).

5.9 Future Interests and Challenges

The large DSN antennas saw a significant evolution in performance during the last three decades of the 20th century. Size was increased from 64 to 70 m, efficiencies were enhanced through dual-reflector shaping, operational frequencies were upgraded from S-band to X-band, and a decision was made to add Ka-band. There was also a growth from single-frequency to multifrequency operation. On the other hand, as the designs have matured, it has become more and more difficult to enhance antenna performance. For example, it is unlikely that antennas will grow physically larger; rather, when needed, additional aperture will be achieved by arraying, that is, by combining the signals from several other DSN antennas or enlisting the aid of other non-DSN radio astronomy antennas. It is also unlikely that X-band efficiency will increase much beyond its present performance. The most significant improvement will likely be made by moving operational frequencies from X-band to Ka-band. The most significant Ka-band problem is with 70-m antenna gain performance versus elevation angle, where the drop-off is large (>5 dB). Several techniques for compensating for this drop-off have been described in this chapter. The next logical step will be to implement one of the compensation systems on the 70-m antenna, thus enabling its use at Ka-band.

References

- [1] Technical staff, Tracking and Data Acquisition Organization, *The NASA/JPL 64-Meter-Diameter Antenna at Goldstone, California: Project Report*, Technical Memorandum 33-671, Jet Propulsion Laboratory, Pasadena, California, July 1974.
- [2] P. D. Potter, "The Application of the Cassegrain Principle to Ground Antennas for Space Communications," *IRE Transactions on Space Electronics and Telemetry*, vol. SET-8, pp. 154–158, June 1962.
- [3] P. D. Potter, *The Design of a Very High Power, Very Low Noise Cassegrain Feed System for Planetary Radar*, Technical Report 32-653, Jet Propulsion Laboratory, Pasadena, California, August 1964.
- [4] P. D. Potter, "A New Horn Antenna with Suppressed Sidelobes and Equal Beamwidth," *Microwave Journal*, vol. VI, no. 6, pp. 71–78, June 1963.
- [5] P. D. Potter, *A Simple Beamshaping Device for Cassegrainian Antennas*, Technical Report 32-214, Jet Propulsion Laboratory, Pasadena, California, January 1962.
- [6] P. Foldes and S. G. Komlos, "Theoretical and Experimental Study of Wideband Paraboloid Antenna with Central Reflector Feed," *RCA Review*, vol. XXI, pp. 94–116, March 1960.
- [7] D. A. Bathker, *Radio Frequency Performance of an 85-ft Ground Antenna: X-Band*, Technical Report 32-1300, Jet Propulsion Laboratory, Pasadena, California, July 1968.
- [8] D. A. Bathker, *Radio Frequency Performance of a 210-ft Ground Antenna: X-Band*, Technical Report 32-1417, Jet Propulsion Laboratory, Pasadena, California, December 1969.
- [9] A. J. Freiley, *Radio Frequency Performance of DSS-14 64-m Antenna at 3.56- and 1.96-cm Wavelengths*, Technical Report 32-1526, vol. XIX, November and December 1973, http://tmo.jpl.nasa.gov/progress_report/issues.html Accessed August 2001.
- [10] W. V. T. Rusch, "Scattering from a Hyperboloidal Reflector in a Cassegrainian Feed System," *IEEE Transactions on Antennas and Propagation*, vol. AP-11, no. 4, pp. 414–421, July 1963.
- [11] W. V. T. Rusch, "Phase Error and Associated Cross-Polarization Effects in Cassegrainian-Fed Microwave Antennas," *IEEE Transactions on Antennas and Propagation*, vol. AP-14, no. 3, pp. 266–275, May 1966.
- [12] STAIR (Structural Analysis Interpretive Routine), Lincoln Manual 40, Massachusetts Institute of Technology Lincoln Laboratory, Lexington, Massachusetts, March 1962.

- [13] J. Ruze, *Physical Limitations on Antennas*, Technical Report 248, Research Laboratory of Electronics, Massachusetts Institute of Technology, Cambridge, Massachusetts, October 1952.
- [14] S. A. Brunstein, "A New Wideband Feed Horn with Equal E- and H-plane Beamwidths and Suppressed Sidelobes," in *Space Programs Summary 37-58, Vol. II, The Deep Space Network*, pp. 61–64, Jet Propulsion Laboratory, Pasadena, California, July 1969.
- [15] H. C. Minnett, B. Thomas, and A. Mac, "A Method of Synthesizing Radiation Patterns with Axial Symmetry," *IEEE Transactions on Antennas and Propagation*, vol. AP-14, no. 5, pp. 654–656, September 1966.
- [16] A. C. Ludwig, "Antennas for Space Communication," in *Space Programs Summary 37-33, Vol. IV, Supporting Research and Advanced Development*, pp. 261–266, June 30, 1965.
- [17] R. F. Thomas, D. A. Bathker, "A Dual Hybrid Mode Feedhorn for DSN Antenna Performance Enhancement," *The Deep Space Network Progress Report 42-22*, vol. May and June 1964, http://tmo.jpl.nasa.gov/progress_report/issues.html Accessed August 2001.
- [18] R. Hartop, "X-Band Antenna Feed Cone Assembly," *The Deep Space Network Progress Report*, November and December 1973, Technical Report 32-1526, vol. XIX, http://tmo.jpl.nasa.gov/progress_report/issues.html Accessed August 2001.
- [19] R. Hartop, "Selectable Polarization at X-Band," *The Deep Space Network Progress Report 42-39*, March and April 1977, http://tmo.jpl.nasa.gov/progress_report/issues.html Accessed August 2001.
- [20] R. Hartop, "New X-Band Microwave Equipment at the DSN 64-meter Stations," *The Deep Space Network Progress Report 42-48*, vol. September and October 1978, http://tmo.jpl.nasa.gov/progress_report/issues.html Accessed August 2001.
- [21] R. W. Hartop, "New X-Band Antenna Feed for DSN 64-meter Stations," *The Deep Space Network Progress Report 42-52*, vol. May and June 1979, http://tmo.jpl.nasa.gov/progress_report/issues.html Accessed August 2001.
- [22] A. J. Freiley, "Radio Frequency Performance of DSS-14 64-m Antenna at X-Band Using a Dual Hybrid Mode Feed," *The Deep Space Network Progress Report 42-53*, July and August 1979, http://tmo.jpl.nasa.gov/progress_report/issues.html Accessed August 2001.
- [23] P. D. Potter, *S- and X-Band RF Feed System*, Technical Report 32-1526, vol. VIII, November and December 1972, http://tmo.jpl.nasa.gov/progress_report/issues.html Accessed August 2001.

- [24] A. C. Ludwig, *Calculation of Scattered Patterns From Asymmetrical Reflectors*, Technical Report 32-1430, Jet Propulsion Laboratory, Pasadena, California, February 15, 1970.
- [25] D. A. Bathker, "Dual Frequency Dichroic Feed Performance," Proceedings 139, AGARD Conference on Antennas for Avionics, June 1974.
- [26] A. C. Ludwig, "Spherical Wave Theory," in *The Handbook of Antenna Design, Volumes 1 and 2* (A. W. Rudge, K. Milne, A. D. Olver, and P. Knight, editors), London: Peter Peregrinus Ltd., pp. 101–123, 1986.
- [27] P. D. Potter, "Application of Spherical Wave Theory to Cassegrainian-Fed Paraboloids," *IEEE Transactions on Antennas and Propagation*, vol. AP-15, no. 6, pp. 727–736, November 1967.
- [28] A. C. Ludwig, "Near-Field Far-Field Transformations Using Spherical-Wave Expansions," *IEEE Transactions on Antennas and Propagation*, vol. AP-19, no. 2, pp. 214–220, March 1971.
- [29] R. T. Woo, "A Low-Loss Circularly Polarized Dichroic Plate," *IEEE G-AP 1971 International Symposium Digest*, pp. 149–152.
- [30] P. D. Potter, *S- and X-Band Feed System*, Technical Report 32-1526, vol. XV, Jet Propulsion Laboratory, Pasadena, California, pp. 54–62, June 15, 1973.
- [31] C. T. Stelzried, "The Venus Balloon Project," *Tracking and Data Acquisition Progress Report 42-80*, vol. October–December 1984, http://tmo.jpl.nasa.gov/progress_report/issues.html Accessed February 13, 2002.
- [32] J. Withington, "DSN 64-meter Antenna L-band (1668-MHz) Microwave System Performance Overview," *Tracking and Data Acquisition Progress Report 42-94*, vol. April–June 1988, http://tmo.jpl.nasa.gov/progress_report/issues.html Accessed February 13, 2002.
- [33] P. H. Stanton and H. F. Reilly, Jr., "The L-/C-band Feed Design for the DSS-14 70-meter Antenna (Phobos Mission)," *Tracking and Data Acquisition Progress Report 42-107*, vol. July–September 1991, http://tmo.jpl.nasa.gov/progress_report/issues.html Accessed February 13, 2002.
- [34] M. S. Gatti, A. J. Freiley, and D. Girdner, "RF Performance Measurement of the DSS-14 70-meter at C-band/L-band," *Tracking and Data Acquisition Progress Report 42-96*, vol. October–December 1988, http://tmo.jpl.nasa.gov/progress_report/issues.html Accessed February 13, 2002.
- [35] D. J. Rochblatt, "A Methodology for Diagnostic and Performance Improvement for Large Reflector and Beam-Waveguide Antennas Using

- Microwave Holography,” *Proceedings of 1991 Symposium of Antenna Mechanical Techniques Association*, pp. 1-7–1-12, October 7–11, 1991.
- [36] D. A. Bathker, A. G. Cha, W. A. Imbriale, W. F. Williams, “Proposed Design and Performance Analysis of NASA/JPL 70-M Dual Reflector Antennas,” *IEEE AP-S International Symposium*, Boston, Massachusetts, June 1984.
 - [37] T. Veruttipong, V. Galindo-Israel, and W. A. Imbriale, “Low-Loss Offset Feeds for Electrically Large Symmetric Dual-Reflector Antennas,” *IEEE Transactions on Antennas and Propagation*, vol. AP-35, no. 7, July 1987.
 - [38] W. F. Williams, “Considerations for Determining the Shaped Main Reflector for the DSN 70-m Upgrade Program,” Telecommunications and Data Acquisition document 890-170, JPL D-1875 (internal document), Jet Propulsion Laboratory, Pasadena, California, November 1984.
 - [39] A. G. Cha, and W. A. Imbriale, “70-m Antenna Reflector Surface Computer Programs,” JPL D-1843 (internal document), Jet Propulsion Laboratory, Pasadena, California, November 1984.
 - [40] A. G. Cha, “Physical Optics Analysis of NASA/JPL Deep Space 70-m Antennas,” JPL D-1853 (internal document), Jet Propulsion Laboratory, Pasadena, California, November 1984.
 - [41] F. Manshadi and R. Hartop, “Compound-Taper Feedhorn for NASA 70-m Antennas,” *IEEE Transactions on Antennas and Propagation*, vol. AP-36, no. 9, September 1988.
 - [42] D. A. Bathker, A. G. Cha, D. J. Rochblatt, B. C. Seidel, and S. D. Slobin, “70-Meter Deep Space Network Antenna Upgrade Performance,” *Proceedings of ISAP*, 1989.
 - [43] M. S. Gatti, M. J. Klein, T. B. H. Kuiper, “32-GHz Performance of the DSS-14 70-meter Antenna: 1989 Configuration,” *Telecommunications and Data Acquisition Progress Report 42-99*, vol. July–September 1989, http://tmo.jpl.nasa.gov/progress_report/issues.html Accessed August 2001.
 - [44] Manshadi, F., “The New Ultra Low Noise Diplexed X-band Microwave Feed for NASA 70-m Antennas,” 2000 IEEE Aerospace Conference Proceedings, Big Sky, Montana, March 18–25, 2000.
 - [45] Epp, L. W., Stanton, P. H., Jorgenson, R. E., and Mittra, R., “Experimental Verification of an Integral Equation Solution for Thin-Walled Dichroic Plate with Cross-shaped Holes,” *IEEE Trans. Antennas and Propagation*, vol. 42, pp. 878–882, June 1994.
 - [46] Britcliffe, M. J. and Fernandez, J. E., “Noise-Temperature Measurements of Deep Space Network Dichroic Plates at 8.4 GHz,” *Telecommunications and Mission Operations Progress Report 42-145*, vol. January–March

- 2001, http://tmo.jpl.nasa.gov/progress_report/issues.html Accessed August 2001.
- [47] R. J. Lacasse, Green Bank Telescope Memo 184, <http://info.gb.nrao.edu/GBT/GBT.html> Accessed August 2001.
- [48] M. Djobadze, J. Kibler, and M. Pryor, "ARISE Subreflector Demonstration Article Final Report," Composite Optics, Inc., internal memorandum, November 23, 1999.
- [49] V. Galindo-Israel, S. R. Rengarajan, W. Veruttipong, and W. A. Imbriale, "Design of a Correcting Plate for Compensating the Main Reflector Distortions of a Dual Shaped System," *IEEE Antennas and Propagation Society International Symposium*, Ann Arbor, Michigan, pp. 246–249, June 1993.
- [50] W. A. Imbriale, M. Moore, D. J. Rochblatt, and W. Veruttipong, "Compensation of Gravity-Induced Structural Deformations on a Beam-Waveguide Antenna Using a Deformable Mirror," *IEEE Antennas and Propagation Society International Symposium 1995*, Newport Beach, California, pp. 1680–1683, June 1995.
- [51] R. Bruno, W. Imbriale, M. Moore, and S. Stewart, "Implementation of a gravity compensating mirror on a large aperture antenna," *AIAA Multidisciplinary Analysis and Optimization*, Bellevue, Washington, September 1996.
- [52] S. R. Rengarajan, W. A. Imbriale, and P. W. Cramer, Jr., "Design of a Deformed Flat Plate to Compensate the Gain Loss Due to the Gravity-Induced Surface Distortion of Large Reflector Antennas," *International Symposium on Electromagnetic Theory*, Thessaloniki, Greece, May 1998, pp. 124–126.
- [53] S. R. Rengarajan and W. A. Imbriale, "A Study of a Deformable Flat Plate for Compensating Reflector Distortions," *USNC URSI Meeting*, Orlando, Florida, pp. 181, July 1999.
- [54] P. Richter, M. Franco, and D. Rochblatt, "Data Analysis and Results of the Ka-Band Array Feed Compensation System/Deformable Flat Plate Experiment at DSS 14," *Telecommunications and Mission Operations Progress Report 42-139*, vol. July–September 1999, Jet Propulsion Laboratory, Pasadena, California, pp. 1–29, http://tmo.jpl.nasa.gov/progress_report/issues.html Accessed August 2001.
- [55] W. A. Imbriale, and D. J. Hoppe, "Computational Methods and Theoretical Results for the Ka-Band Array Feed Compensation System/Deformable Flat Plate Experiment at DSS 14," *Telecommunications and Mission Operations Progress Report 42-140*, vol. October–December 1999, http://tmo.jpl.nasa.gov/progress_report/issues.html Accessed August 2001.

- [56] V. Vilnrotter, E. Rodemich, and S. Dolinar, Jr., "Real-time Combining of Residual Carrier Array Signals Using ML Weight Estimates," *IEEE Transactions on Communications*, vol. 40, pp. 604–615, 1992.
- [57] V. Vilnrotter, D. Fort, and B. Iijima, "Real-time Array Feed System Demonstration at JPL," in *Multifeed Systems for Radio Telescopes*, Astronomical Society of the Pacific Conference Series, vol. 75, pp. 61–73, 1995.
- [58] V. Vilnrotter and D. Fort "Demonstration and Evaluation of the Ka-Band Array Feed Compensation System on the 70-Meter Antenna at DSS 14," *Telecommunications and Mission Operations Progress Report 42-139*, vol. July to September 1999, http://tmo.jpl.nasa.gov/progress_report/issues.html Accessed August 2001.
- [59] D. Rochblatt and V. Vilnrotter, "Demonstration of a Ka-band Array Feed-Deformable Flat Plate Compensation System," *TMOD Technology and Science Program News*, Issue 12, Jet Propulsion Laboratory, Pasadena, California, June 2000.
- [60] W. Imbriale, D. Hoppe, and D. Rochblatt, "Analysis of the DFP/AFCS System for Compensating Gravity Distortions on the 70-meter Antenna," International Symposium for Deep Space Communications and Navigation, Pasadena, California, September 21, 1999.
- [61] D. Hoppe, "70-meter Ka-band Implementation Study," JPL D-19434, Jet Propulsion Laboratory, Pasadena, California, January 10, 2000.
- [62] W. A. Imbriale, and D. J. Hoppe, "Advances in the Deep Space Network—Adding Ka-band to the 70-meter Antenna," URSI meeting, Boulder, Colorado, January 2000.
- [63] D. J. Rochblatt, D. Hoppe, W. Imbriale, M. Franco, P. Richter, P. Withington, and H. Jackson, "A Methodology for the Open Loop Calibration of a Deformable Flat Plate on a 70-meter Antenna," *Proceedings of the Millennium Conference on Antennas Propagation AP2000*, Davos, Switzerland, 2000.